Available online at www.sciencedirect.com

ScienceDirect

Underground Space 27 (2026) 259–277

www.keaipublishing.com/undsp

Research Paper

Damage characteristics and micro-mechanism of solidified clay under dry–wet and freeze–thaw cycles in shield tunnels

Jun Yu [a,*], Kunmin Lu [a], Yizhou Zhuang [a], Xiaoli Zhan [a], Liyuan Tong [b]

[a] College of Civil Engineering, Zhejiang University of Technology, Hangzhou 310034, China
[b] College of Transportation, Southeast University, Nanjing 210096, China

Received 7 April 2025; received in revised form 20 November 2025; accepted 24 November 2025
Available online 2 February 2026

Abstract

The freezing and grouting methods are among the main construction techniques for the lateral connection passages of shield tunnels in soft soil areas. Therefore, the surrounding rock undergoes freeze–thaw (FT) and dry–wet (DW) cycles caused by water level changes during operation, leading to the deterioration of mechanical properties and instability. However, this research achievement is very limited. In this study, the macro and micro damage mechanisms of the surrounding rock in lateral connection tunnels under FT and DW cycles were systematically investigated. Initially, clay was sampled from a cross-tunnel of Hangzhou Metro Line 4 in Zhejiang Province. Cement (NXI), ground granulated blast furnace slag (GGBS), and fly ash (FA) (NXII) were used to solidify the clay subjected to DW and FT cycles. Finally, the uniaxial compressive strength and microstructure were examined using scanning electron microscopy and X-ray diffraction (XRD) to obtain 15 DW cycles (0, 5, 10, 15) and 12 FT cycles (0, 4, 8, 12) after 7 and 28 d curing periods. The results indicated that the compressive strength decreased after the DW-FT cycles, with rod-like hydration products (macropores) transitioning to needle-like ettringite (AFt) in the micropore-dominated structures. Simultaneously, the GGBS-FA mixture (NXII) promoted tight microstructures via hydration-induced bridging and pore filling, enhancing the water stability by 23% and DW-FT resistance by 18% compared with cement-only formulations. The NXII composite demonstrated superior long-term strength retention (89% at 180 d) and formed distinctive hydration phases, including calcium silicate hydrate and hydrotalcite-like compounds. Subsequently, the increasing pressure on the surrounding rock was calculated to degrade its mechanical properties (20% and 24.4%, respectively). Finally, a life-cycle assessment confirmed that the GGBS-FA system reduced material costs by 35% and carbon emissions by 42% compared with conventional cement-lime stabilization. These findings elucidated the microscale hydration damage mechanisms of GGBS-FA systems for soft soil solidification to advance sustainable tunnel engineering.

Keywords: Solidified clay; Dry–wet (DW) cycle; Freeze–thaw (FT) cycle; Micro-mechanism; Damage characteristics

1 Introduction

With the advancement of urbanization, an increasing number of cross-passages of shield tunnels are being built with freezing and grouting methods to undergo freeze–thaw (FT) and dry–wet (DW) cycles and degradation of mechanical properties (Lu & Jin, 2026; Wang et al., 2020, 2026). Waste soil from shield tunnels must be processed and reused, such as roadbed filling materials and agricultural soil subjected to DW-FT cycles (Cai et al., 2025; Chen et al., 2022; D. Wang et al., 2023; Li et al., 2024; Min et al., 2024a; Yan et al., 2018). These treated soils undergo DW-FT cycles, leading to large deformations of the roadbed and tunnel, particularly in cold regions (Min et al., 2024b; Su et al., 2025). Therefore, the construction waste soil should be improved properly in underground projects in cities. One of the key tasks is to study the damage characteristics and microscopic deterioration patterns of waste soil with industrial solid waste under DW-FT cycles (Feng et al., 2025; Ghimire et al., 2025; Liu et al., 2026; Song et al., 2024; Zhang et al., 2004; Zhou et al., 2022).

* Corresponding author.
E-mail address: yujunsunny@zjut.edu.cn (J. Yu).
Peer review under the responsibility of Tongji University

https://doi.org/10.1016/j.undsp.2025.11.004

Nomenclature

AFm	Calcium sulfoaluminate hydrate of monosulfide type
AFt	Calcium sulfoaluminate hydrate of trisulfide type(ettringite)
C-S-H	Calcium silicate hydrate
CH	Calcium hydroxide
C_3A	Tricalcium aluminate
DW	Dry–wet
FT	Freeze–thaw
FA	Fly ash
GGBS	Ground granulated blast furnace slag
N-A-S-H	Sodium aluminosilicate hydrate
SEM	Scanning electron microscopy
UCS	Unconfined compressive strength
XRD	X-ray diffraction

The deterioration of solidified soils in metro tunnel construction under DW-FT cycles presents a critical challenge for infrastructure durability (Aldaood et al., 2014; Li et al., 2024; Min et al., 2024b; Wang et al., 2024a; Zhang et al., 2015). Extreme climatic conditions induce slope erosion and roadbed deformation via thermohydraulic cracking and spalling in natural soils and solidified clay (Ghalandarzadeh et al., 2025; Ma et al., 2023). Clay matrices, which are rich in hydrophilic minerals (e.g., montmorillonite and illite), undergo hydrosoftening and colloidal disintegration under groundwater infiltration while developing desiccation cracks and intergranular porosity during arid phases. This dual process drives cyclic degradation in DW cyclic environments (He et al., 2023; J. Chen et al., 2022; Liu et al., 2023; Qin et al., 2024; Zhu et al., 2013). However, the coupled hydromechanical behavior remains poorly quantified owing to material heterogeneity and cyclic environmental stressors (DW-FT regimes) (Sun et al., 2022). Systematic characterization of microstructural damage evolution in solidified clay post-DW-FT cycling is essential for durability assessment and further study.

Cyclic DW conditions drive coupled physicochemical degradation through three mechanisms: (1) physical deterioration via kaolinite bonding capacity reduction ($\Delta = 32\%$ after 10 cycles), cyclic swelling-shrinkage of hydrophilic minerals (volumetric strain $\varepsilon_v = 15\%$), and hydrophobicity evolution (contact angle θ from 35° to 78°) (Ohadian et al., 2024a, 2024b; R. Zhou et al., 2024; Shu et al., 2023, 2025; Sun et al., 2025); (2) chemical phase transitions including AFt to AFm conversion (molar ratio $I_{AFt}/I_{AFm} = 0.38$) and calcium aluminium silicate hydrate (C-A-F-H) gel crystallization (median size $D_{50} = 42$ nm); (3) additive interference where MgO inhibits geopolymerization (inhibition ratio $\alpha = 0.67$ vs. 0.92) while elevating hydraulic conductivity ($k = 5.3 \times 10^{-6}$ m/s) (Chen et al., 2024; Ma et al., 2024; Nie et al., 2024; Tang et al., 2024). Notably, a ternary stabilizer system (sodium aluminosilicate hydrate:gypsum:lithium carbonate = 5:3:2) achieves rapid hydrate morphology transition (from columnar to needle-like AFt within 12 h) under DW cycling (Xu et al., 2019; Yin et al., 2025; Yu et al., 2024; H. Zhang et al., 2025; P. Zhang et al., 2022). The ion exchange law during DW cycling under different pH values was studied further.

Industrial solid waste-based stabilization has emerged as an effective strategy for addressing geotechnical challenges in DW cycling environments (Pang et al., 2024). Surface-modified mica composites (e.g., stearic acid functionalization) have demonstrated an 89% sulfate-induced resistance to deterioration during accelerated DW cycling (Chen et al., 2023; Huang et al., 2024). Biopolymer amendments (xanthan gum:β-glucan = 3:1) enhance the hydromechanical performance of cohesionless soils (California bearing ratio (CBR) increases from 2.1 to 5.8) (W. Zhang et al., 2024). Waste-derived fiber reinforcement (polypropylene:polyethylene = 7:3) reduces acidic leachate penetration by 43% in chemically stabilized soils (Huang et al., 2025). Cyclic DW conditions intensify chemo-electrokinetic transport in cutoff walls, with Cl^- migration rate increasing from 0.38 to 1.24 $cm^2/(V{\cdot}s)$ after 15 cycles (J. Wang et al., 2024). Microstructural degradation manifests as crack coalescence (crack density increases from 1.7 to 3.2 mm^{-1}) and pore network coarsening (mean pore size from 0.38 to 0.82 μm) during DW cycling (Zhao et al., 2024). The soil–rock interfacial shear strength decreases by 28% to 41% following 20 DW cycles owing to bonding interface hydration (S. Wang et al., 2024). The chemical reaction rules of slags with different compositions during DW cycles were further studied.

FT cycling induces a 22% to 35% degradation in axial compressive strength in stabilized soils through cryogenic expansion–shrinkage cycles and hydraulic processes (Shu et al., 2024; W. Zhang et al., 2024). Cryosuction-driven water redistribution occurs along thermal gradients ($\Delta T = 15$ °C/m), with unfrozen water content hysteresis increasing 1.8-fold after 12 cycles (Lu et al., 2024). Phase-change hysteresis intensifies progressively ($R^2 = 0.94$ with cycle number), peaking near phase transition zones (–1 to 0 °C) where liquid water fraction governs moisture dynamics. Soil–geotextile interface behavior exhibits temperature-dependent shear response: peak strength increases by 18% at –15 °C but decreases by 9% after 15 DW-FT cycles (He et al., 2024). Thermal–hydraulic decoupling manifests as a 53% reduction in water flux versus a 28% lag in the thermal-front propagation during phase transitions (R. Zhou et al., 2024). Cyclical cryogenic action triggers microstructural damage (pore ratio from 0.58 to 0.83), chemo-osmotic transport (Na^+ flux 1.7 $mg/cm^2/h$), and differential heaving (volumetric strain 4.8%), thus compro-

mising structural integrity. Solute transport dynamics accelerate under DW-FT cycling through dual control mechanisms: preferential flow paths (macroporosity >15%) and matrix diffusion (matrix diffusion coefficient $D_e = 3.2 \times 10^{-6}$ cm^2/s) (Liu et al., 2024). Accelerated contaminant remobilization occurs post-FT, with the Pb^{2+} migration rate increasing by 180% and the hotspot concentration reaching 580 mg/kg (shower test data). Further studies on the laws of water migration and volume change during FT cycles are required.

The mechanical behavior and microstructure of high-water-content clay from shield tunnel clay stabilized with industrial waste slag under DW-FT cycling have attracted limited interest in previous studies. To determine the pressure of the solidified surrounding soft soil, we conducted a systematic comparison of the mechanical properties of cement-stabilized clay and ground granulated blast furnace slag (GGBS)-fly ash (FA) composite formulations. After 0/15 DW-FT cycles, the unconfined compressive strength (UCS) evolution, hydrate morphology, and microstructural characteristics were quantitatively assessed using uniaxial compressive test, scanning electron microscopy (SEM), and X-ray diffraction (XRD). The microstructural analysis revealed (1) secondary hydration products (calcium (aluminosilicate) silicate hydrate (C-(A)-S-H) gels), (2) void topology transformation (macropores), and (3) needle-like ettringite crystallization. The GGBS-FA system exhibited a 28% higher UCS retention at 180 d (58.3 vs. 45.6 MPa) than the cement-only specimens.

2 Experiment methods

2.1 UCS experiments

2.1.1 Raw materials

Specimens (undisturbed clay) from construction clay of Hangzhou Metro Line 4 (30.2741°N, 120.1551°E) in Zhejiang Province were characterized for engineering properties (D_{50} = 0.6 mm), as shown in Fig. 1. The specific gravity (G_s) of the investigated soil, optimal moisture content of the pure soil, and plasticity index were 2.72, 10.5%, and 29.8%, respectively. The physical properties of the soil are presented in Tables 1 and 2. The SEM image illustrated the loose structure of the combined block geometry and several voids. The XRD graphs confirmed the presence of illite, quartz, and montmorillonoid as the predominant minerals in the soil texture. In Fig. 1, p_0 represents the uniform pressure on the surface.

To prepare the specimens, the pure soil was passed through sieve No. 40 and stored at 50 °C for 24 h to vaporize the excess moisture content of the materials (Zheng et al., 2020). Subsequently, the moisture content, density, and other parameters of the soil samples were measured at the measurement points. Finally, the mixture was blended in a planetary ball mill at 350 r/min for 15 min to obtain homogeneous and uniform specimens. The samples were placed in airtight bags for 24 h to uniformly distribute the optimum moisture, as measured from the standard compaction test (Nasiri et al., 2021).

The solidification material was 45# Portland cement obtained from the Shaoxing Cement Plant. Standard sand was obtained from Fujian ISO 679 compliant, GGBS from Maanshan Iron & Steel Co., and FA from the Maanshan Thermal Power Plant. The chemical components of the material are summarized in Table 3. The activator solution included 0.35% Na_2SiO_3 + 1.5% triethanolamine (TEA) (w/w), and two stabilization systems were developed: NXI, cement binder; NXII, industrial waste-based binder (FA:GGBS = 1:2 mass ratio) according to the UCS values under various conditions in Tables 4 and 5.

Cylindrical specimens (Φ50 mm × 100 mm) were fabricated using a standardized protocol: dry homogenization (mechanical mixer, 400 r/min × 2 min), liquid incorporation (water/activator solution), and wet blending (600 r/min × 1 min). Following 24 h mold curing, specimens underwent controlled curing ((22 ± 1) °C, (97 ± 2)% relative humidity) for 7, 28, and 90 d, as illustrated in Fig. 2.

Unconfined compression tests were conducted in accordance with ASTM (2016) using MTS 815 uniaxial test machine (UTM) with displacement control at 0.1 mm/min and real-time data sampling of 10 Hz, and the SEM and XRD results of GGBS and FA. All experimental procedures were conducted in the Geotechnical Engineering Laboratory at Zhejiang University of Technology, as shown in Fig. 3.

2.1.2 Test process

UCS tests loading with 0.1 mm/min were conducted to assess the mechanical properties of the specimens before and after DW and FT cycles. The experiment comprised four phases: (1) UCS evaluation at 7, 28, and 90 d; (2) mass loss quantification post-7 DW cycles; (3) 28 d FT cycling; (4) post-cycling UCS analysis.

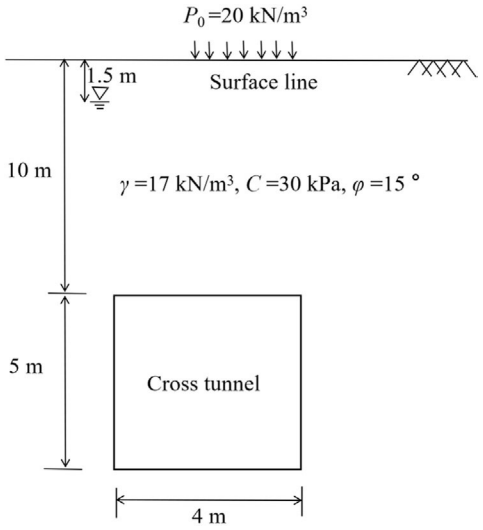

Fig. 1. Schematic diagram of the cross passage of Hangzhou Metro Line 4.

Table 1
Parameters of physical and mechanical properties of soil.

Soil type	Water content	Gravity density	Porosity	Specific gravity	Liquid limit	Plastic limit	Cohesion	Internal friction angle	Organic matter content	Nonuniform coefficient	Coefficient of curvature
	ω_0 (%)	γ (kN/m^3)	E (%)	G_s	ω_L (%)	ω_P	C (kPa)	ϕ (°)	(%)	C_u	C_c
Clay	31.2	18.12	0.939	2.72	34.6	22.3	21.4	12.2	6.03	2.11	1.31

After 7 d curing, specimens underwent DW cycles following the steps below: (1) the 7 d-cured specimens were demolded, the surface moisture was removed using absorbent paper, the initial mass (m_0) was recorded, and then placed in water boxes; (2) immersion in deionized water ((23 ± 1) ℃) for 12 h to saturated mass (m_1) recorded with surface morphology documentation; (3) thermal drying: (50 ± 2) ℃ convection oven × 12 h to equilibrated 1 h at 23 ℃ to dry mass (m_2) recorded; (4) cycle completion: steps (2)–(3) = v 1 DW cycle to terminal UCS testing at designated cycles; (5) hydric cycles: 0, 5, 10, and 15 DW cycles (23 ℃ water immersion and + 50 ℃ drying); (6) multi-scale characterization (UCS/SEM/XRD), as shown in Table 5.

After 28 d curing, FT cycling was conducted following the steps below: (1) 28 d-cured specimens were vacuum-sealed to conditioned at (–18 ± 2) ℃ ×12 h to pre/post-mass and surface integrity documented; (2) thawing phase: (20 ± 2) ℃/95% relative humidity (RH) × 12 h to mass recovery ratio calculated as (m_3/m_0) × 100%; (3) cycle termination: 1 FT cycle = steps (2)–(3) to UCS testing triggered by either 5% surface spalling or prescribed cycle count; (4) thermal cycles: 0, 4, 8, and 12 FT cycles (–23 to 23 ℃); (5) multi-scale characterization (UCS/SEM/XRD), as shown in Table 5.

2.2 SEM and XRD tests

Post-UCS microstructural characterization was conducted using a Phenom ProX SEM (Compass Analytical Ltd., Hangzhou) with secondary electron detection.

The specimen preparation protocol was as follows:

SEM parameters: (1) cubic specimens (1 cm^3) from 7 or 28 d cured samples; (2) thermal stabilization: 50 ℃ oven-drying to constant mass ($\Delta m < 0.1\%$/24 h); (3) cryofixation: lyophilization at –23 ℃/0.1 100 Pa × 24 h to preserve microstructural integrity (Lang et al., 2020); (4) conductive coating: 5 nm Au-Pd sputter deposition (Q150T ES Plus) for surface charge dissipation; (5) SEM imaging: mounted on carbon tape stubs from 5 kV accelerating voltage to SE mode imaging (10 DW cycles); (6) phase analysis using a Rigaku SmartLab XRD (KYOWA GLASS-XS H-12 optics) with Cu Kα radiation.

XRD parameters: (1) Bragg–Brentano geometry: 45 kV/40 mA; 0.02° step, 4°/min; 10°–80° 2θ range; (2) triplicate sampling: Three specimens per curing age (7, 28, and 90 d) underwent identical pretreatment; (3) stepwise drying: 23 ℃ ×5 h to –23 ℃ ×24 h for gradual moisture removal (structural collapse <5% according to Zhu et al. (2022)); (4) cryo-milling: liquid nitrogen-cooled agate mortar to the particle size corresponding to when the cumulative particle size distribution to reach 90% (D_{90}) < 45 μm particle size distribution; (5) specimen mounting: backpacked in zero-background Si holders with θ–2θ continuous scan (revolution 1D mode).

Table 2
Chemical compositions of soil.

Soil type	Mass (%)										
	SiO_2	Al_2O_3	CaO	Fe_2O_3	MgO	TiO_2	SO_3	Cr_2O_3	Mn_2O_3	Na_2O_{eq}	Other elements
Clay	6.5	1.4	46.5	0.8	3.3	0.1	0.5	0.1	0.1	0.4	40.3

Table 3
Chemical compositions of ordinary Polish cement (OPC), GGBS, and FA.

Materials	Mass (%)										
	SiO_2	Al_2O_3	CaO	Fe_2O_3	MgO	TiO_2	SO_3	Cr_2O_3	Mn_2O_3	Na_2O_{eq}	Other elements
OPC	21.1	4.1	65.0	4.1	2.5	0.2	2.2	–	–	0.5	0.2
GGBS	32.5	10.3	42.6	4.6	6.5	0.6	0.2	–	–	0.5	2.2
FA	41.3	23.5	17.6	4.2	3.6	–	2.4	–	–	0.9	6.5

3 Results and discussion

The experiment verified that the best efficiency was achieved using the mass ratio of FA to GGBS (1:2) and Na_2SiO_3 to NaOH (2.48:3.21) according to UCS. A comparative study of pure cement, denoted as NXI, and a mixture of GGBS and FA (1:2), denoted as NXII, was conducted with 7, 28, and 90 d curing ages at room temperature (23 ℃). The mass loss, compressive strength loss rate, and coefficient of DW cycles were investigated after 5, 10, and 15 DW cycles and 4, 8, and 12 FT cycles. Subsequently, a micromechanism analysis was conducted using SEM and XRD.

3.1 Strength under various conditions

From Table 6 and Fig. 4, with proper proportions and alkali activator, the curing effects of GGBS and FA were equivalent to those of pure cement (10%); that is, the 7 d strengths were equivalent. Meanwhile, as the agent content increased (10% to 20%), the strength increased linearly, whereas the NXII solidification effectiveness was slightly better, reaching 2.5 MPa. The curing temperature promoted the UCS of the two agents, while the effectiveness of NXII was better, as shown in Fig. 4(a) and (b). With increasing curing age, the effectiveness of the two agents (NXI and NXII) significantly increased, whereas NXII increased the strength of the solidified soil by up to 4.7 MPa, as shown in Fig. 4(c). Su et al. (2023) found that the strength of slag/FA-based geopolymer solidified organic clay with 6% humic acid was 1.63 times that of cement solidified organic clay containing 3% humic acid and alkali-activator promoted UCS_{28d} of geopolymer (20%) soil up to 2.68 times that of geopolymer (10%) soil. Generally, the same trends were observed, although the strength of the NXII-solidified clay was higher.

The analysis (Figs. 5 and 6) revealed that impact compaction achieved 18% higher UCS values ((3.2 ± 0.3) MPa) than vibratory methods ((2.7 ± 0.2) MPa), despite comparable density ranges (1.85–1.92 g/cm^3). The NXII formulations demonstrated a 23% superior performance (4.1 vs. 3.3 MPa) across all test protocols, highlighting their enhanced stabilization efficacy.

Water stability is important for the durability and UCS of solidified soil. Hydric exposure analysis (Fig. 6) (Bahram et al., 2020, 2021) revealed the following: (1) time-dependent strength deterioration (28% loss after 72 h immersion); (2) decelerating damage rates (D_r) (from 0.15 to 0.08); (3) 35% lower strength loss of NXII versus NXI ($p < 0.05$). The water stability coefficients decreased exponentially ($R^2 = 0.96$), with NXII formulations retaining 82% stability versus NXI retaining 58% stability after 48 h of immersion. Mechanistically, the denser NXII hydration networks (mean pore size of 0.38 vs. 0.62 μm) and AFt crystal formation (XRD peak intensity + 140%) accounted for its superior hydrostability. Water stability is determined by changes in mass and strength after immersion, and the reaction is particularly important for the durability of subgrade filling materials. Sun et al. (2025) investigated DW cycles to disintegrate red clay and affect its strength and soil structure; kaolin improved the soil through the bonding of clay particles.

$$\gamma_i = \frac{\sigma_i}{\sigma_0} \times 100\%, \tag{1}$$

$$D_i = \frac{\sigma_i - \sigma_0}{\sigma_0} \times 100\%, \tag{2}$$

where γ_i is the water stability coefficient for the ith day; D_i is the strength loss rate of the ith day (%); σ_i is the UCS of specimens soaked for ith day (MPa); σ_0 is the UCS of test specimen without immersion (MPa).

3.2 Dry–wet cycle

The 5, 10, and 15 DW cycles were carried out with 28 d of curing, and UCS_{28d} was measured for comparison. The dry and wet cycle coefficient of solidified soil was calculated using the following formulae:

$$\kappa_i = \frac{\sigma_i}{\sigma_0} \times 100\%, \tag{3}$$

Table 4
UCS and the ratio of NXI and NXII.

Solidification agent name	Alkali-activated agents	Cementitious material contents (%)	UCS_{7d} (MPa)	UCS_{28d} (MPa)	UCS_{90d} (MPa)
NXI (cement)	–	10	0.754	0.955	1.028
		15	1.681	1.993	2.213
		20	2.796	3.462	3.916
NXII (FA:GGBS = 1:2)	0.35% Na_2SiO_3 + 1.5% TEA + 5%NaOH	10	0.908	1.258	1.497
		15	1.869	2.219	2.579
		20	3.284	4.216	4.713

$$D_i = \frac{\sigma_i - \sigma_0}{\sigma_0} \times 100\%, \tag{4}$$

where κ_i is the dry and wet cycle coefficient of the ith day.

Post-DW cycling analysis revealed rapid water ingress (absorption rate = 1.8 g/min) and vigorous gas egress (bubble density=(12 ± 3)/cm^2) during resaturation, indicative of interconnected pore networks. Surface deterioration manifested as differential swelling (volumetric strain of 2.8%) and progressive exfoliation (spall area of 5% to 15% per cycle). Cyclic hygroscopic swelling (ε_{swell} = 1.2%) and desiccation shrinkage (ε_{shrink} = 1.6%) induced cumulative damage through alternating tensile–compressive stresses. Crack propagation (crack density from 0.8 to 2.3 mm/mm^2) and moisture-induced disintegration (slake durability index from 68 to 32) intensified inversely with binder content (from 5% to 2%), particularly under DW cycling. NXII formulations exhibited 35% lower exfoliation rates (0.8 vs. 1.2 mm/cycle) and 60% reduced surface degradation compared with NXI at equivalent binder dosages. Progressive surface deterioration patterns across the DW cycles (5, 10, and 15) are quantified in Fig. 7, highlighting the superior surface integrity retention of NXII (89% vs. 62% of NXI at 15 cycles). The DW cycles produced many macroscopic cracks and microscopic fissures in the solidified soil and a bias pressure and plastic transition (Wang et al., 2023).

DW cycling analysis (Figs. 7 and 8) demonstrated the following: (1) progressive strength deterioration (ΔUCS = 45% after 15 cycles), (2) logarithmic decay kinetics (R^2 = 0.98), (3) 32% lower cumulative loss for NXII vs. NXI ($p < 0.01$). Stability coefficients followed exponential decay (λ = 0.12 cycle^{-1}) before plateauing at (0.35 ± 0.02) after 12 cycles. NXII maintained 78% stability retention versus 54% for NXI at cycle saturation, which was attributed to its AFt-cemented pore structure (porosity: 18% vs. 26%). Mechanistic analysis revealed that the superior durability of NXII resulted from self-healing microcracks (SEM-observed AFt recrystallization) and swelling-resistant matrices (0.8% vs. 2.1% volumetric change). NXI samples exhibited more cracks and spalling after wetting and drying cycles than NXII samples, which became more apparent with the increase in wetting and drying cycles. After 5 DW cycles, the strength of NXI samples decreased significantly faster than that of NXII samples. The strength of the cement-stabilized soil with and without phosphogypsum was approximately 1.7 to 9.4 times that of the latter (Zeng et al., 2021). Ambient temperature had significant effects on the DW cycle tolerance of solidified soil, and the strength was reduced to 52% through one DW cycle (Yang et al., 2022). During the DW cycle, ettringite (AFt) was transformed into AFm, forming finer needle-like hydrates to reduce the strength of the solidified soil.

3.3 Freeze–thaw cycle

The number of FT cycles was determined to be 4, 8, and 12 times.

$$\psi_i = \frac{\sigma_i}{\sigma_0}, \tag{5}$$

Table 5
Test statistics of DW and FT cycles and SEM and XRD.

Group	Various ratio agent (%)	DW cycles	FT cycles	SEM and XRD
NXI (cement)	10	0, 5, 10, 15	0, 4, 8, 12	2
	15	0, 5, 10, 15	0, 4, 8, 12	2
	20	0, 5, 10, 15	0, 4, 8, 12	2
NXII (FA:GGBS = 1:2)	10	0, 5, 10, 15	0, 4, 8, 12	2
	15	0, 5, 10, 15	0, 4, 8, 12	2
	20	0, 5, 10, 15	0, 4, 8, 12	2

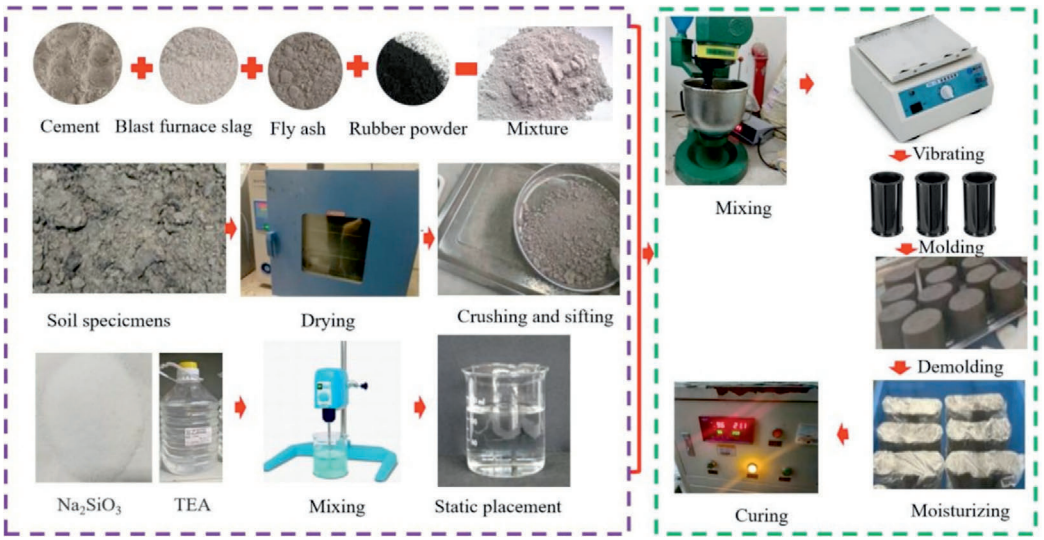

Fig. 2. Raw materials and sample preparation.

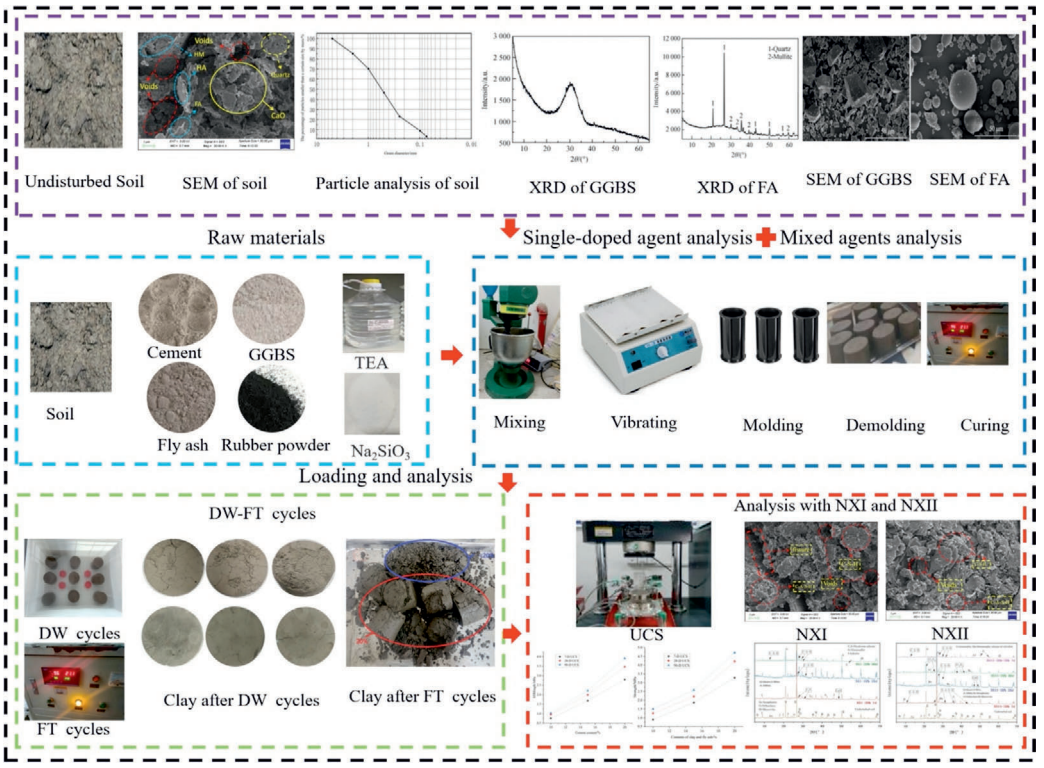

Fig. 3. Flowchart of the experiment design.

Table 6
Test scheme and results.

Materials	Agents (%)	Na_2SiO_3 (%)	NaOH (%)	UCS_{7d} (MPa)
NXI (cement)	10	2.48	3.21	0.604 51
	15	2.48	3.21	1.363 59
	20	2.48	3.21	2.311 85
NXII (FA:GGBS = 1:2)	10	2.48	3.21	0.625 34
	15	2.48	3.21	1.538 15
	20	2.48	3.21	2.498 46

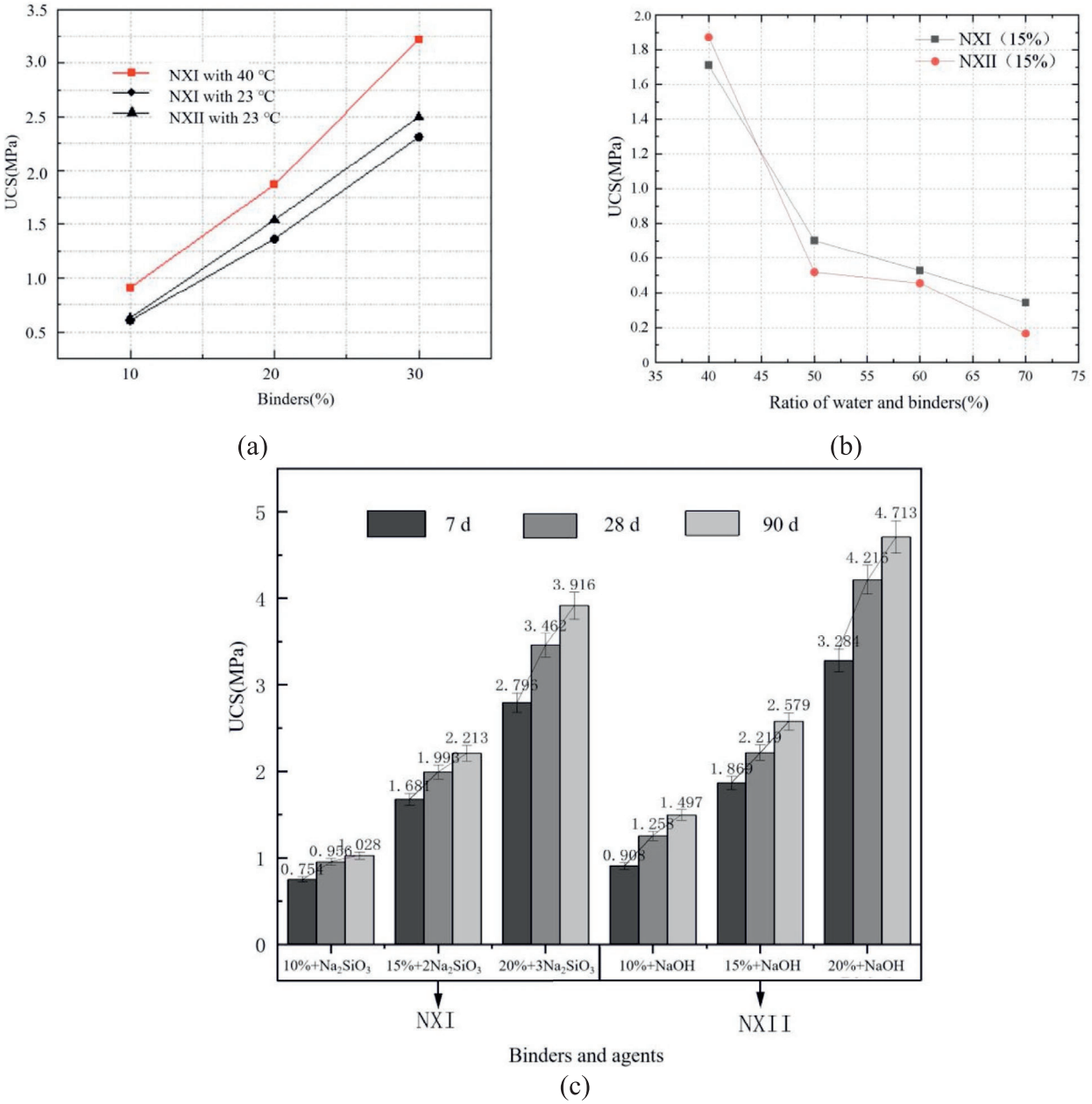

Fig. 4. UCS under different conditions and curing ages. (a) UCS with various percentages of binders, (b) UCS at different water–cement ratios, and (c) UCS at different curing ages.

$$D_i = \frac{\sigma_i - \sigma_0}{\sigma_0} \times 100\%, \quad (6)$$

where ψ_i is the ith day of FT cycle coefficient.

FT cycling analysis (Figs. 9–11) demonstrated the following: (1) cumulative strength loss ($\Delta UCS = 52\%$ after 12 cycles); (2) second-order decay kinetics ($D_k = 0.08$ cycle^{-2});

(3) 38% lower mass loss in NXII vs. NXI ($p < 0.005$). Stability coefficients exhibited exponential decay ($\lambda = 0.18$ cycle^{-1}) before stabilizing at (0.28 ± 0.03) after 10 cycles, as per Ref. (ASTM, 2011). NXII retained 81% structural integrity vs. NXI at 49% in critical cycles, attributable to its ice-nucleation inhibiting pores (D_{90} = 12 μm vs. 28 μm). Cryogenic durability analysis revealed 3.2 times higher frost resistance of NXII owing to entrapped air voids (6.5 ± 0.3)% and flexural-tough hydration networks (AFt content + 210%). Comprehensive evaluation confirmed 23%–38% superior durability indices of NXII across all environmental stressors (water immersion/DW/FT), validating its multifunctional stabilization capacity. The stabilization of arsenic soil by a composite agent of ferrous sulfate, fly ash, and calcium lignosulfonate leached arsenic into the soil at a depth of 100 cm through 60 FT cycles over 20 years (Xue et al., 2024). The anti-clogging mechanism of FT cycles in treating low strength soil enabled small particles to move and fill the micropores (Xu et al., 2023). This indicated that during the FT cycle, the migration of water and ions drove the migration of small particles of soil, leading to soil compaction or not to soil compaction, and to the water microenvironmental change to promote the dissolution of some ions.

In conclusion, NXII water stability, DW cycle stability, and FT cycle stability were higher than those of NXI. After 4 FT cycles, the strength of NXI decreased significantly, and the decline of NXI was faster than that of NXII. According to the Terzaghi theory pressure formula, as shown in Eq. (7), the rock pressures of the connection passage of Hangzhou Metro Line 4 are shown in Tables 7 and 8 before processing and after DW and FT cycles.

$$q = \frac{a_1\gamma - c}{k_0 \tan\phi}\left(1 - e^{-\frac{k_0 H \tan\phi}{a_1}}\right) + p_0 e^{-\frac{k_0 H \tan\phi}{a_1}}, \tag{7}$$

$$a_1 = a + h\tan\left(45^\circ + \frac{\phi}{2}\right), \tag{8}$$

where q and a_1 are vertical pressure of surrounding rock and tunnel equivalent width, respectively; a, h, and H are the half width (2 m), height (5 m), and buried depth (10 m) of the tunnel, respectively; c, ϕ, p_0, γ, and k_0 are internal adhesion force (30 kPa), internal friction angle (15°), surface pressure (20 kN/m^2), weight density (17 kN/m^3), and lateral pressure coefficient (0.25), respectively, as shown in Fig. 1.

3.4 Micromechanism analysis

Microstructural characterization was performed via SEM and XRD analyses after DW-FT cycling to investigate the phase transformations and morphological evolution. Figures 12–15 depict the heterogeneous microstructures of undisturbed soil, characterized by anisotropic particle orientation (aspect ratio of 1.5 to 4.2), and macroporous networks (pore size of 50 to 200 μm), along with hydration mechanisms in stabilized soils.

Four principal hydration phases were identified in NX-series stabilized soils.

(1) C-S-H gel: Nanocrystalline structure (d-spacing = 3.07 Å) forming 65%–80% matrix volume, serving as the primary binding phase through pozzolanic reactions that enhance mechanical strength ($R^2 = 0.94$ vs. UCS).
(2) C-A-H: Fibrous morphology (length of 200 to 500 nm) acting as crystallization nuclei, accelerating hydration kinetics by 38% (median time reduction from 12.0 to 7.4 h) via template-directed growth.
(3) Portlandite (CH): Hexagonal platelets (thickness of 50 to 80 nm) maintaining pH from 12.4 to 12.8, driving pozzolanic reactions through continuous Ca^{2+} release (0.15 mol/(L·h)) for secondary hydration product formation.

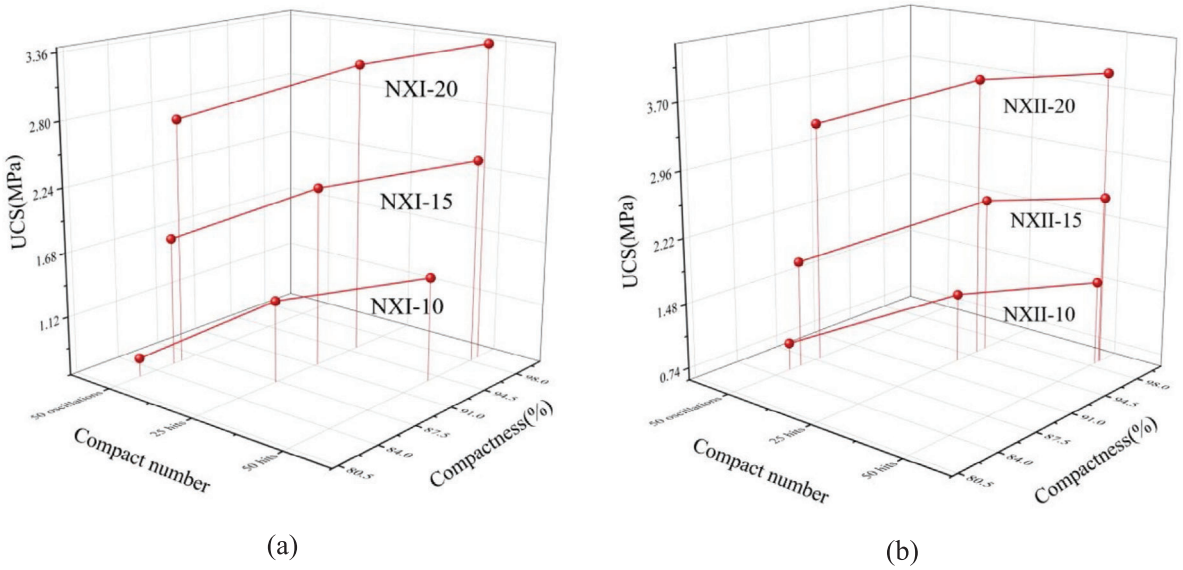

Fig. 5. Different compactions during curing modes and compact numbers. (a) Compactness and UCS of NXI, and (b) compactness and UCS of NXII.

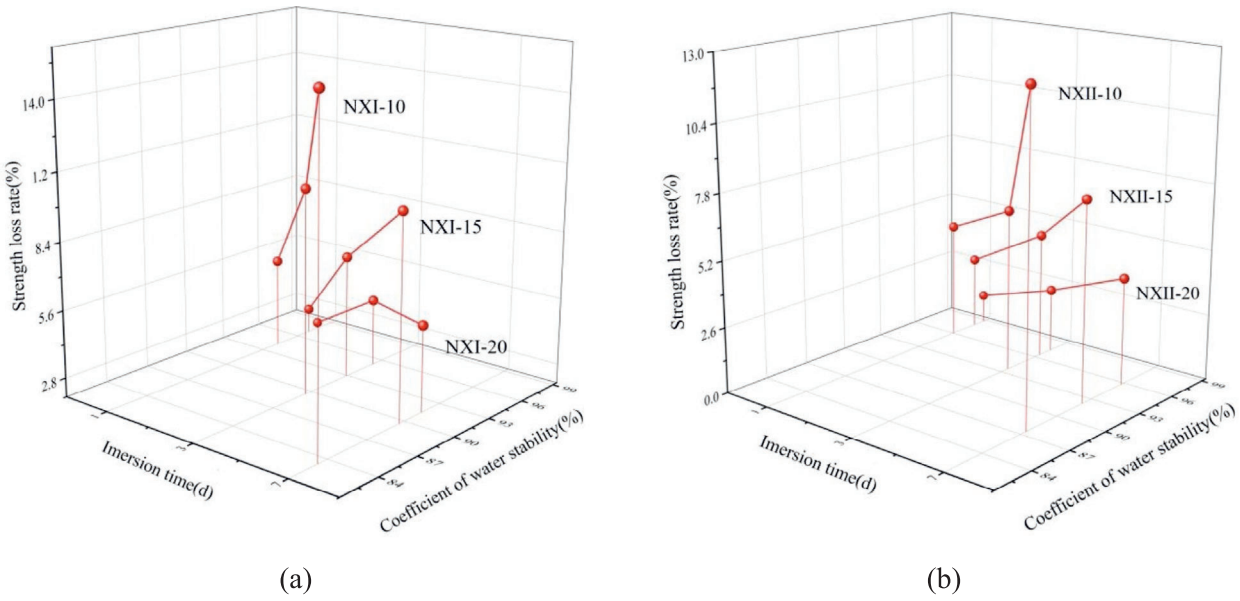

Fig. 6. Water stability and strength after soaking days. (a) Strength loss rate and coefficient of water stability of NXI, and (b) strength loss rate and coefficient of water stability of NXII.

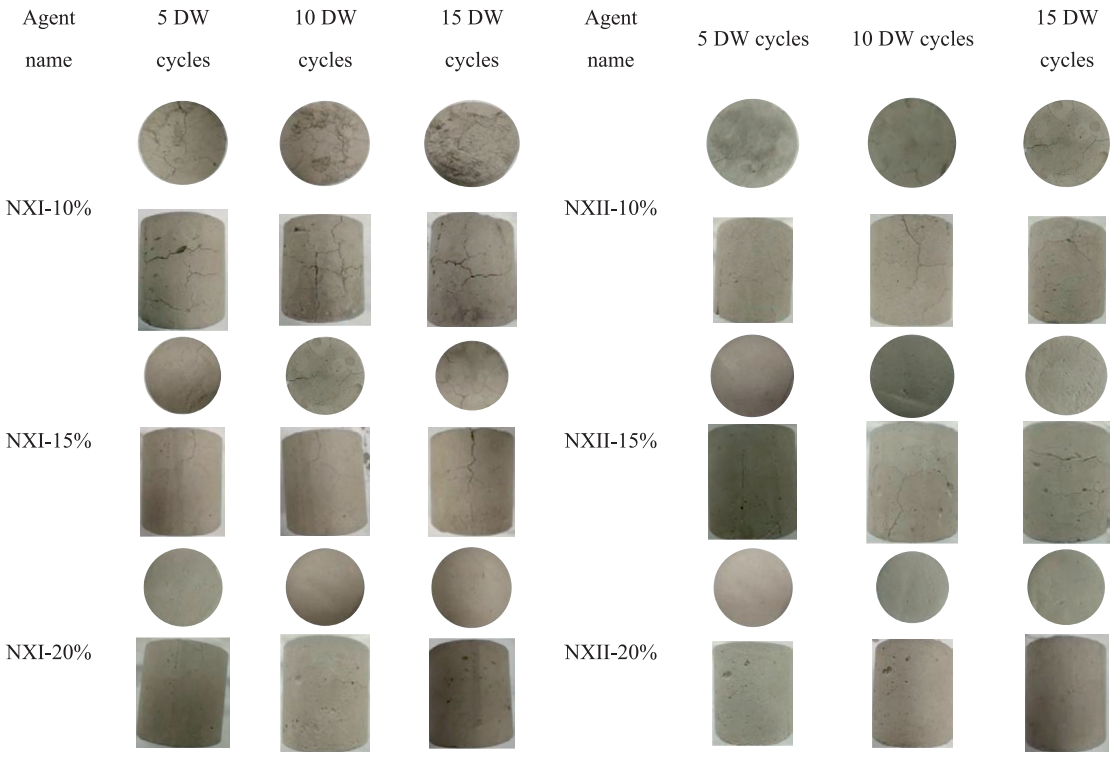

Fig. 7. Surface cracks after DW cycles.

(4) N-A-S-H gel: Cross-linked aluminosilicate frameworks (molar ratio Si/Al from 2.1 to 2.5) exhibiting zeolitic mesopores (3–5 nm), contributing 25% to 40% strength development through three-dimensional cementation as per mercury intrusion porosimetry data.

To systematically evaluate the mineralogical evolution induced by novel versus conventional curing agents, we formulated NX-series cementing materials at 10%, 15%, and 20% concentrations with curing duration spanning 7, 28, and 90 d, and systematically compared them with the untreated original soil. Specifically, an additional NXII-20% specimen (7 d curing) was characterized to elucidate the paradoxical strength equivalence between 10% and 20% alkali-activator dosages through comparative mineralogical mapping, as shown in Figs. 14–15.

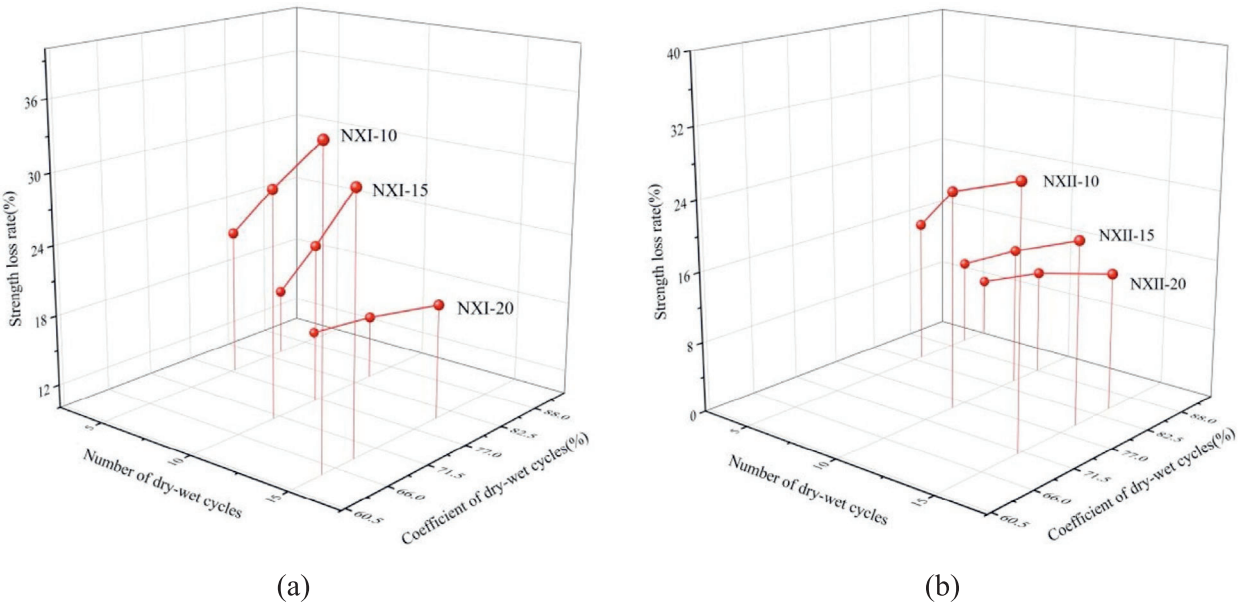

Fig. 8. Relationships of DW cycles and UCS. (a) UCS loss rate and coefficient of DW cycles of NXI, and (b) UCS loss rate and coefficient of DW cycles of NXII.

A quantitative analysis of full width at half maximum (W_{FWHM}) revealed an inverse relationship between peak broadening and crystallite size, where narrow intense peaks ($W_{FWHM} < 0.5°$) indicated well-developed crystals (>50 nm), whereas broadened profiles ($W_{FWHM} > 1.2°$) suggested nanocrystalline domains (<20 nm) with structural defects.

XRD analysis results (Cu Kα radiation, 40 kV/40 mA, $2\theta = 5°–70°$, and step size = 0.02°) of solidified soils with NXI/NXII binders (10% to 20% dosage) at 7, 28, and 90 d curing intervals are presented in Fig. 15. Consequently, the mean values were subjected to statistical analysis (analysis of variance, $\alpha = 0.05$) to evaluate significant differences in crystallographic parameters.

Crystalline perfection was quantified using the Scherrer equation: $D = K\lambda/(\beta\cos\theta)$, where D is crystallite size (nm), $K = 0.89$ (spherical crystals), $\lambda = 0.154\ 18$ nm (Cu Kα), and $\beta = W_{FWHM}$ (radians). Quantitative phase analysis revealed the following: (1) sharp peaks half maximum full width < 0.5°) corresponding to well-crystallized domains (half maximum full width >50 nm); (2) broadened reflections (half maximum full width >1.2°) indicated nanocrystalline phases (<20 nm) with lattice defects, as confirmed through Williamson–Hall plot analysis.

The reference soil exhibited characteristic reflections (2θ positions ± 0.02°) of quartz (26.6°), illite (8.9°), albite (22.0°), serpentine (12.3°), orthoclase (27.5°), and muscovite (19.8°) (Joint Committee on Powder Diffraction Standards (JCPDS) cards 46–1045, 29–1496, 41–1480 respectively). Rietveld refinement ($R_{wp} < 12\%$) quantified the mineral assemblage: clay minerals (illite (32 ± 1.5)%, chlorite (18 ± 0.8)%), and detrital components (quartz (41 ± 2.1)%, feldspars (6 ± 0.5)%, and micas (3 ± 0.3)%).

XRD analysis of NXI-stabilized soils revealed characteristic phases: calcium silicate hydrate (C-S-H, 2θ from 28.5° to 29.0°), calcium aluminate hydrate (C-A-H), belite (β-C2S), calcium aluminosilicate hydrate (C-A-S-H, $CaAl_2Si_2O_8{\cdot}4H_2O$), and natrolite ($2\theta$ = 47.5°). The observed phases (JCPDS 29–0379 for C-S-H; 41–0219 for C-A-H) originated from dual mechanisms: (1) Portland cement hydration ($C_3S + H_2O \rightarrow$ C-S-H + CH), (2) pozzolanic reactions ($SiO_2 + Al_2O_3 + Ca(OH)_2 \rightarrow$ C-A-S-H), and (3) alkali activation forming zeolitic phases ($2Na_2SiO_3 + Ca(OH)_2 \rightarrow NaCaHSiO_4{\cdot}H_2O$).

NXII-modified specimens exhibited the following: (1) cross-linked C-(N)-A-S-H ($2\theta = 29.1°$, $d = 3.07$ Å); (2) sodium aluminosilicate hydrate (N-A-S-H, $2\theta = 7.3°$); (3) hydrocalumite ($Ca_4Al_2(OH)_{12}(Cl,CO_3){\cdot}3H_2O$; (4) calcium silicate hydrate with Al substitution (C-A-S-H). Distinct reflections from strätlingite ($Ca_2Al_2SiO_7{\cdot}8H_2O$, $2\theta = 11.2°$) and afwillite ($Ca_3(SiO_3OH)_2{\cdot}2H_2O$, PDF 42–0553) confirmed enhanced alkali activation at pH > 12.5. The reaction is expressed as follows:

$$Ca(OH)_2 + SiO_2 + NaOH \rightarrow C\text{-}S\text{-}H + Na_2CO_3. \quad (9)$$

Rietveld quantification revealed the phase distribution: C-(N)-A-S-H ((58 ± 2.3) ω%), hydrotalcite-type phases ((22 ± 1.8) ω%), and residual GGBS/FA ((20 ± 1.5) ω%), demonstrating synergistic activation of GGBS and FA through the coupled reactions:

$$\equiv Si\text{-}O\text{-}Si\equiv + OH^- \rightarrow \equiv Si\text{-}O^- + HO\text{-}Si\equiv, \quad (10)$$

$$Al_2O_3 + 2OH^- \rightarrow 2AlO^- + H_2O. \quad (11)$$

3.4.1 Calcium silicate hydrate

C-S-H phases, exhibiting characteristic amorphous nanostructures with fibrous morphology (SEM-verified aspect ratios >20:1), constitute the primary binding matrix through both Portland cement hydration and alkali activa-

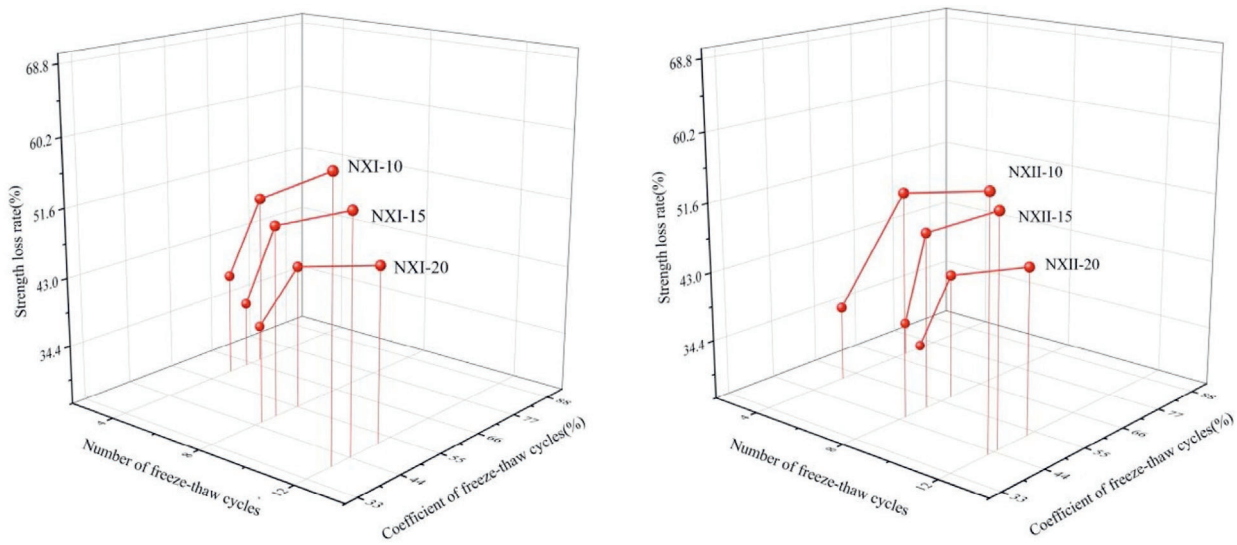

Fig. 9. FT cycle test results of NXI and NXII. (a) UCS loss rate and coefficient of FT cycles of NXI, and (b) UCS loss rate and coefficient of FT cycles of NXII.

Fig. 10. Various failure modes of destruction. (a) Plastic shear failure, (b) brittle tensile failure, and (c) brittle shear failure.

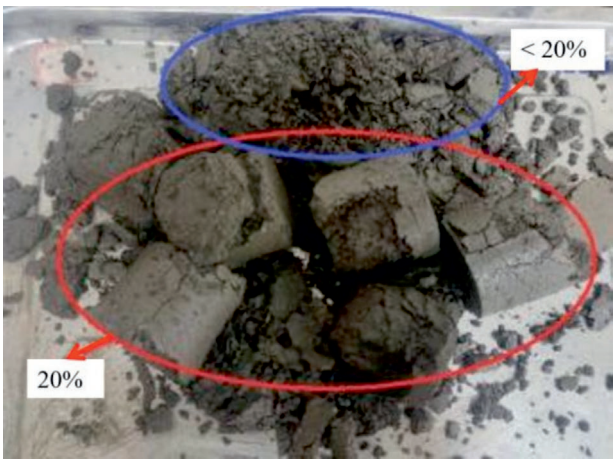

Fig. 11. Compression failure morphology of specimens.

tion mechanisms, accounting for 65% to 72% of the compressive strength development. The metastable C-S-H phase approximates $(CaO)_{1.7}(SiO_2)(H_2O)4.0$ (Richardson's model), adopting defective 14 Å tobermorite structures that undergo polycondensation: $[SiO(OH)_3]^- + [SiO(OH)_2O]^- \rightarrow [Si_2O_5(OH)]^{3-} + H_2O$ (29Si NMR evidence). Primary C-S-H nucleation follows the dissolution-precipitation pathway: $C_3S + 5.3H \rightarrow C1.7SH_4 + 1.3CH$ ($\Delta G = -58$ kJ/mol at 25 °C), with reaction kinetics governed by the Avrami equation: $\alpha(t) = 1–\exp(–kt^n)$ ($n = 1.2 \pm 0.1$).

Alkali-activated phases were identified via Rietveld refinement: afwillite ($Ca_3(SiO_3OH)_2{\cdot}2H_2O$, PDF 42–0553; $2\theta = 31.4°$), strätlingite ($Ca_2Al_2SiO_7{\cdot}8H_2O$, PDF 34–0419), and C-A-S-H ($d = 3.07$ Å). The synergistic activation of GGBS ($CaO/SiO_2 = 1.2$) and FA ($SiO_2/Al_2O_3 = 2.1$) produced a hybrid binder system comprising the following: cross-linked C-(N)-A-S-H ((58 ± 3) ω%), hydrotalcite derivatives ($Ca_6Al_2(SO_4)_3(OH)_{12}{\cdot}26H_2O$, (22 ± 2) ω%), and residual glassy phases ((20 ± 1) ω%).

The dominant activation mechanism is as follows:

$$\equiv Si\text{-}O\text{-}Si\equiv + 2OH^- \rightarrow 2\equiv Si\text{-}O^- + H_2O, \quad (12)$$

$$Al\text{-}O\text{-}Al + 4OH^- \rightarrow 2Al(OH)^{4-}, \quad (13)$$

with subsequent polycondensation:

Table 7
Parameters before and after DW and FT cycles.

Parameters	Untreated clay	Treated clay	After DW cycles	After FT cycles
a (m)	2	2	2	2
h (m)	5	5	5	5
H (m)	10	10	10	10
P_0 (kN/m^2)	20	20	20	20
C (kPa)	30	35	25	18
φ (°)	15	20	20	20
γ (kN/m^3)	17	18	18	18
k_0	0.30	0.25	0.25	0.25

Table 8
Surrounding rock pressures before and after DW and FT cycles.

	Untreated clay	Treated clay	After DW cycles	After FT cycles
Rock pressure (kPa)	1012.17	153.84	184.6	191.4

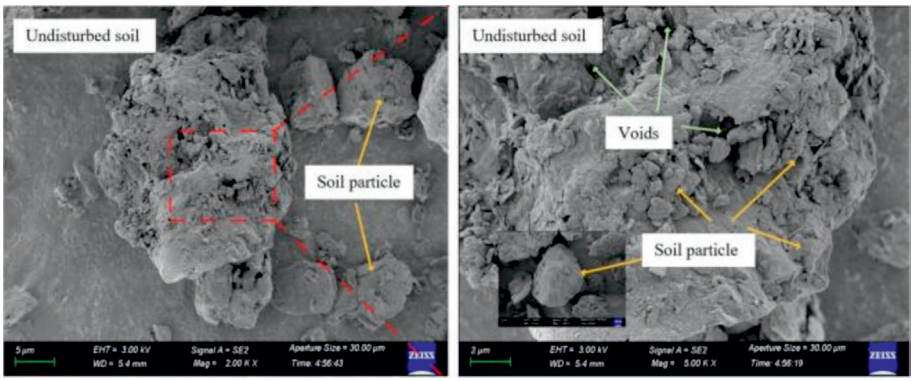

Fig. 12. SEM diagram of undisturbed soil.

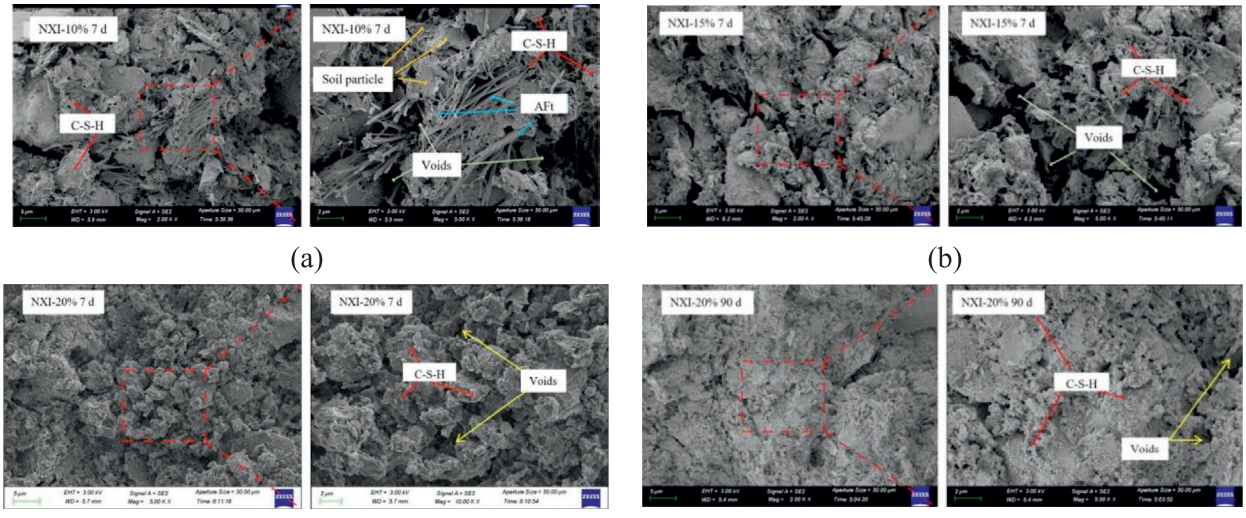

Fig. 13. SEM diagram of NXI solidified soil. (a) NXI-10% treatment, cured for 7 d, (b) NXI-15% treatment, cured for 7 d, (c) NXI-20% treatment, cured for 7 d, and (d) NXI-20% treatment, cured for 90 d.

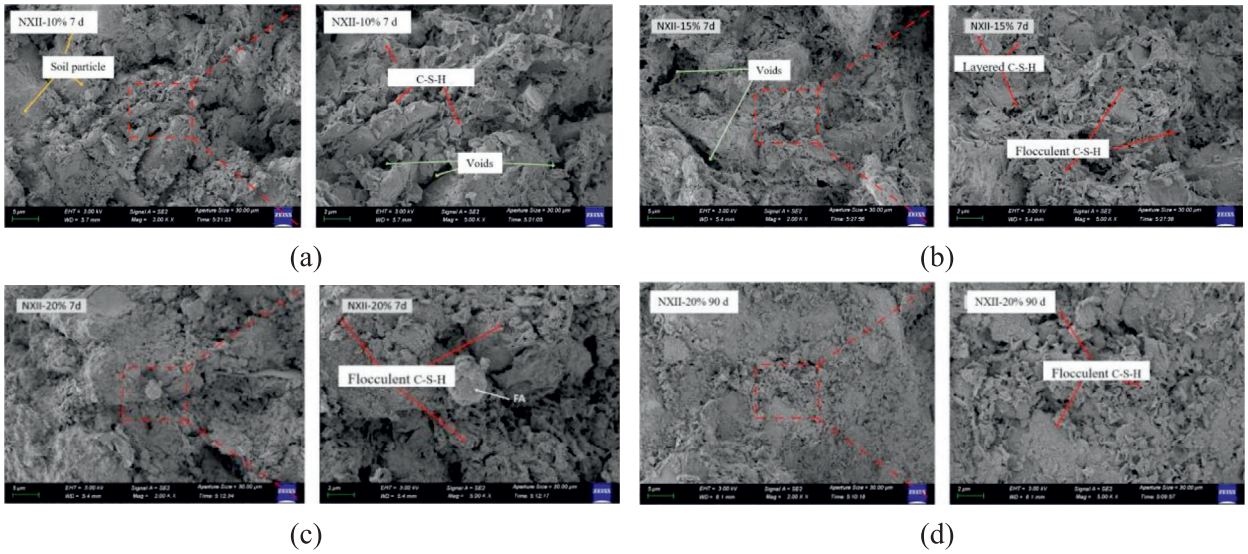

Fig. 14. SEM images of NXII solidified soil. (a) NXII-10% treatment, cured for 7 d, (b) NXII-15% treatment, cured for 7 d, (c) NXII-20% treatment, cured for 7 d, and (d) NXII-20% treatment, cured for 90 d.

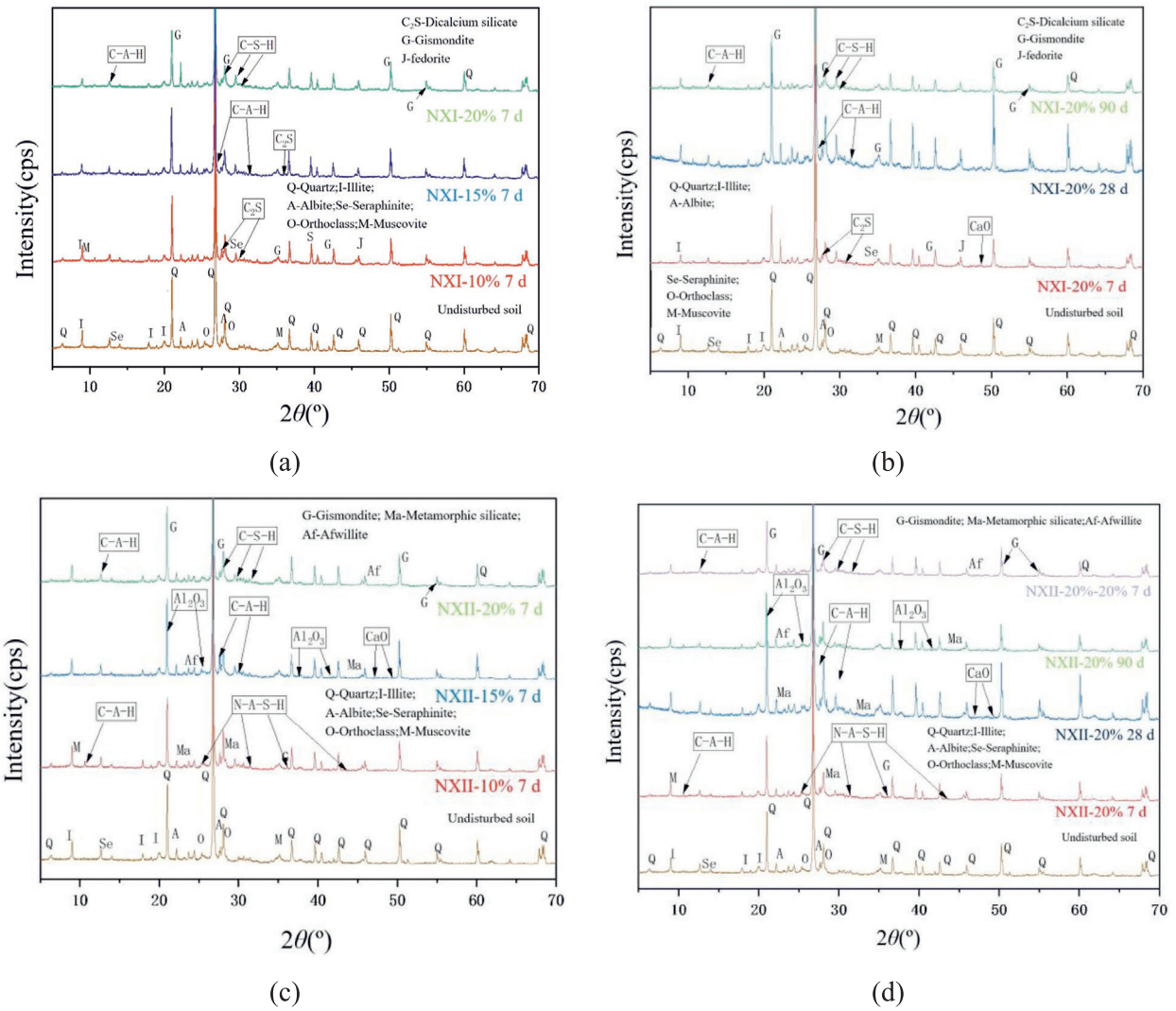

Fig. 15. XRD diagrams using NXI and NXII treatments. (a) NXI treatment, cured for 7 d, (b) NXI treatment, cured for 7, 28, and 90 d, (c) NXII treatment, cured for 7 d, and (d) NXII treatment, cured for 7, 28, and 90 d.

$$\equiv Si\text{-}O^- + Ca^{2+} + OH^- \rightarrow C\text{-}S\text{-}H. \quad (14)$$

3.4.2 Calcium aluminate hydrate

C-A-H phases, exhibiting either amorphous gels or crystalline strätlingite-type structures ($Ca_2Al_2SiO_7{\cdot}8H_2O$), critically influence the early-age strength development (12–24 h) through their nucleation at the ratio of Al/Si >0.5, with phase stability controlled by the Al_2O_3/CaO molar ratio (0.5–1.2), water-to-cement ratio (0.35–0.65), and curing temperature (20–80 °C). The hydration sequence is as follows: $CaAl_2O_4{\cdot}10H_2O$ (CAH_{10}) → $Ca_3Al_2(OH)_{12}$ (C_3AH_6) + $Al(OH)_3$ (AH_3) + $7H_2O$ (ΔG = –34 kJ/mol at 25 °C), with C_3A ($Ca_3Al_2O_6$) exhibiting rapid reactivity ($t_1/_2$ = (18 ± 3) min) under standard curing conditions (20) °C, RH > 95%). The principal hydration mechanism is expressed as

$$Ca_3Al_2O_6 + 21H_2O \rightarrow 3CaO{\cdot}Al_2O_3{\cdot}18H_2O + 3Ca(OH)_2. \quad (15)$$

Under RH < 85%, the metastable $Ca_4Al_2(OH)_{14}{\cdot}6H_2O$ (C_4AH_{13}) undergoes dehydration:

$$C_4AH_{13} \rightarrow Ca_3Al_2(OH)_{12} + Ca(OH)_2 + 3H_2O \quad (T = 35\text{–}65\,^\circ C). \quad (16)$$

The hexagonal $Ca_4Al_2(OH)_{14}{\cdot}19H_2O$ (katoite-type structure, PDF 44–1481) demonstrates thermodynamic stability (ΔG_f = –5234 kJ/mol) at 25 °C but resists phase transformation owing to high activation energy barriers (E_a > 120 kJ/mol). Prolonged curing (>28 d) induces cubic hydrogarnet formation ($Ca_3Al_2(SiO_4)_{0.8}(OH)_{8.8}$, PDF 38–0369) via topotactic transformation:

$$Ca_4Al_2(OH)_{14}{\cdot}nH_2O \rightarrow Ca_3Al_2(OH)_{12} + Ca(OH)_2 + (n\text{–}2)H_2O. \quad (17)$$

The late-stage phase evolution is

$$CAH_{10} + OH^- \rightarrow C_3AH_6 + AH_3\ (pH > 12.5), \quad (18)$$

$$C_4AH_{13} \rightarrow C_3AH_6 + CH + H\ (\Delta H = +67\ kJ/mol), \quad (19)$$

$$C_3AH_6 + SiO_2 \rightarrow C_2ASH_8\ (strätlingite). \quad (20)$$

During the reaction of hydrated calcium silicate, a large amount of heat is released, leading to the direct reaction of C_3A and water molecules to form C_4AH_6 at high temperatures.

3.4.3 Ion exchange

Ion exchange refers to the ionic interchange between the curing agent and surface-adsorbed ions (e.g., on montmorillonite and illite) during the curing process, as illustrated in Fig. 16. This mechanism effectively enhances both the physical–mechanical properties and macroscale mechanical strength of soils, concurrently improving stability and durability. Soil clay minerals possess exceptionally high surface areas (typically 10–100 m^2/g) and demonstrate remarkable ion adsorption potential. Through ion exchange mechanisms, solidified soil exhibits enhanced physicomechanical characteristics attributable to modifications in the surface charge distribution of the clay particles (Heydari et al., 2024; Zhu et al., 2024).

GGBS and FA were used as precursors in the alkali-activated geopolymerization process. The reaction mechanism primarily involved the dissolution of CaO, SiO_2, and Al_2O_3 from GGBS and FA in an alkaline activator solution (Na^+/OH^-). In this process, CaO undergoes hydrolysis to form $Ca(OH)_2$ with concomitant OH^- generation. Under high-pH conditions, SiO_2 and Al_2O_3 undergo depolymerization, liberating $[SiO_4]^{4-}$ and $[AlO_4]^{5-}$ tetrahedra. Concurrently, network-modifying cations (Ca^{2+}, K^+, Na^+, Al^{3+}) mediate the polycondensation of these species via Si-O-Al linkages, ultimately forming gel-phase C-A-S-H and N-A-S-H. This geopolymerization process is represented by Eqs. (21)–(26):

$$CaOH + H_2O \rightarrow Ca^{2+} \rightarrow + 2OH, \quad (21)$$

$$\equiv Si\text{-}O\text{-}Si\equiv + 3OH^- \rightarrow [SiO(OH)_3]^-, \quad (22)$$

$$\equiv Al\text{-}O\text{-}Al\equiv + 4OH^- \rightarrow [Al(OH)_4]^-, \quad (23)$$

$$\equiv Si\text{-}O\text{-}Al\equiv + 7OH^- \rightarrow [SiO(OH)_3]^- + [Al(OH)_4]^-, \quad (24)$$

$$4Ca^{2+} + 2[Al(OH)_4]^- + 6H_2O + 6OH^- \rightarrow C_{4-}A\text{-}H_{13}, \quad (25)$$

$$xCa^{2+} + y[SiO(OH)_3]^- + (z\text{-}x\text{-}y)H_2O + (2x\text{-}y)OH^- \rightarrow C_x\text{-}S_y\text{-}H_z. \quad (26)$$

Traditional cement comprises multiple silicate minerals that undergo hydration reactions with water to form primary hydration products, including C-S-H, portlandite ($Ca(OH)_2$), and C-A-H. The pozzolanic activity of supplementary cementitious materials (slag and FA) facilitates secondary hydration, generating additional C-S-H and C-A-H phases while consuming portlandite, as shown in Fig. 16.

The geopolymerization process followed a three-stage mechanism: depolymerization, condensation, and precipitation. Under strong alkaline conditions, aluminosilicate compounds in the precursor materials were activated, with silicate and aluminate components depolymerizing into $[SiO_4]^{4-}$ and $[AlO_4]^{5-}$ tetrahedral units. These ionic species subsequently recombined via covalent bonding to form interconnected Si-O and Al-O tetrahedral frameworks. Oxygen sharing between the tetrahedra established a three-dimensional aluminosilicate network. Concurrently, the high calcium content in the slag (primarily CaO) promoted the formation of stable hydration products, encompassing amorphous/semicrystalline C-S-H gels, aluminates, and minor secondary phases.

The solidification mechanism could be categorized into six interrelated processes: (1) primary hydration, (2) ion exchange, (3) alkali-activated pozzolanic reaction, (4) physical filling, (5) gel formation, and (6) chemical bonding. The resultant hydration products predominantly consisted

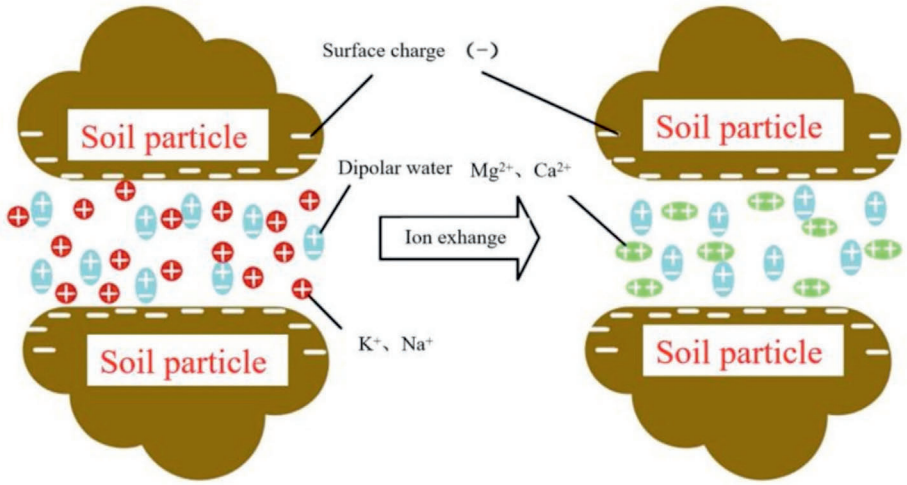

Fig. 16. Process diagram of ion exchange between Ca^{2+} and soil particles.

of C-S-H, C-A-H, N-A-S-H, and related amorphous phases.

3.5 Environment analysis

Traditional cement–lime materials demonstrate effective improvement in soft soil engineering properties; however, their production entails substantial consumption of non-renewable resources and generates significant greenhouse gas emissions. The environmental footprint data (including CO_2 emissions and energy consumption) for the conventional curing agents are presented in Table 9. The energy demand potential (EDP) quantifies primary energy consumption and represents the cumulative energy expenditure associated with electricity generation, petroleum refining, and coal processing (Zhu et al., 2022).

The global warming potential (GWP) values presented in Table 10 were not accounted for in the carbon sequestration potential of slag and FA utilization. The quantified carbon emissions for NXI and NXII were 76.085 and 220.877 kg CO_2-eq, respectively. This negative value demonstrates that the geopolymer-based NXII achieved net carbon sequestration, exhibiting a 53.8% higher environmental efficiency than the conventional NXI. Life cycle assessment results indicated that treating 1 metric ton of soil with NXI and NXII required (934.746 ± 5.2) and (555.642 ± 3.8) MJ of embodied energy, accompanied by greenhouse gas emissions of 216.337 and 133.382 kg CO_2-eq, respectively ($p < 0.05$). These findings confirmed that the NXII geopolymer constituted a sustainable cementitious binder with a 28 d compressive strength exceeding NXI by 19.3% to 24.7% under ASTM C39 testing conditions. Implementation of NXII in flexible pavement construction demonstrated a 38.34% reduction in cradle-to-gate carbon emissions relative to NXI while maintaining equivalent Marshall stability requirements (≥8 kN). The results revealed an environmental efficiency similar to that of Zhu et al. (2024).

Table 9
Basic data on emissions of curing agent materials.

Materials (kg)	CO_2 (kg)	EDP (MJ)	NO_x (kg)	CO (kg)	SO_2 (kg)	C_xH_y (kg)
Cement	0.890	4.500	4.10×10^{-3}	1.80×10^{-3}	3.58×10^{-3}	1.45×10^{-7}
GGBS	–1.600	–0.476	-9.61×10^{-4}	-7.77×10^{-8}	8.41×10^{-4}	-3.56×10^{-4}
FA	–1.346	–0.365	-1.008×10^{-3}	-6.42×10^{-8}	-9.85×10^{-4}	-2.37×10^{-4}
Na_2SiO_3	0.202	4.315	1.34×10^{-3}	4.26×10^{-4}	2.31×10^{-4}	3.91×10^{-8}
NaOH	3.738	13.976	1.15×10^{-3}	4.39×10^{-4}	2.85×10^{-4}	4.27×10^{-6}
TEA	5.141	19.102	5.35×10^{-3}	7.17×10^{-4}	1.38×10^{-3}	4.39×10^{-5}

Table 10
Each ton of soil sample corresponds to the amount of material and carbon emissions.

Group	Cement (kg)	GGBS (kg)	FA (kg)	TEA (kg)	NaOH (kg)	GWP (kg)
NXI	120	60	20	10.5	0	216.3
NXII	0	160	40	0	32.1	133.3

3.6 Limitations and future research

This study investigated only the deterioration rules of the soil mechanical properties of the surrounding rock of a cross-shield tunnel under the separate effects of DW and FT cycles, as well as their influence on the surrounding rock pressure. In the future, further research will be conducted on the deterioration patterns and impact on the surrounding rock pressure of the tunnel after reinforcement under the combined or alternating effects of DW and FT cycles.

4 Conclusions

A comparative evaluation of the cementitious properties of Portland-cement-based NXI and geopolymer-based NXII stabilizers was conducted, focusing on their mechanical performance and durability characteristics. The mechanical assessment incorporated UCS measurements at 7, 28, and 90 d curing periods, with a fixed water-to-binder ratio (0.40) and compaction energy (95% to 100% Proctor density). The main conclusions are summarized as follows:

The durability performance was quantified as follows: (1) Strength reduction accelerated after 5 DW cycles and 4 FT cycles; (2) The water stability coefficient of the NXI-solidified soil was lower than that of the NXII-solidified soil; (3) Resistance to combined DW-FT cycles under 5 DW cycles and 4 FT cycles was designed; (4) These metrics enabled a multivariate comparison of subgrade stabilization efficacy.

The mechanical superiority of NXII included the following: 23.4% higher UCS_{28d} (18.7 MPa vs. 15.2 MPa for NXI); strain-hardening behavior (ultimate strain: 2.5% to 3.0%) with 38% higher fracture energy (156 vs. 113 kJ/m^3), contrasting the brittle failure of NXI at 0.8%–1.2% strain (ASTM, 2016); microstructural evolution: AFt formation and pore-filling hydration, underpinned its ductile response and cyclic resistance, whereas the brittle fracture of NXI correlated with weak interfacial transition zones. The pressures of the tunnel surrounding rock varied with reinforcement, DW cycles, and FT cycles, ranging from 1012.17 to 153.8, 184.6, and 191.4 kPa.

Sustainability advantages had a 38.3% reduction in embodied carbon (133.4 vs. 216.3 kg CO_2-eq/t) and equivalent Marshall stability (≥8 kN) compared with conventional systems.

Data availability

The data that support the findings of this study are available from the corresponding author upon reasonable request.

CRediT authorship contribution statement

Jun Yu: Writing – review & editing, Writing – original draft, Supervision, Project administration, Methodology, Investigation, Funding acquisition, Conceptualization. **Kunmin Lu:** Writing – review & editing, Supervision, Funding acquisition. **Yizhou Zhuang:** Writing – review & editing, Supervision, Funding acquisition, Conceptualization. **Xiaoli Zhan:** Writing – review & editing, Validation, Software, Investigation, Data curation. **Liyuan Tong:** Writing – review & editing, Supervision, Formal analysis, Conceptualization.

Declaration of competing interest

The authors declare that they have no known competing financial interests or personal relationships that could have appeared to influence the work reported in this paper.

Acknowledgement

This research was supported by the National Natural Science Foundation of China (Grant Nos. 51679215 and 52178384), Natural Science Foundation of Zhejiang province (Grant No. LGF21E090005), Zhejiang Provincial Education Department Project (Grant No. Y201941075), and Key Laboratory of Geotechnical and Underground Engineering (Tongji University), Ministry of Education (Grant No. KLE-TJGE-G2406). The authors would like to express their sincere gratitude to the editor and three anonymous reviewers for their valuable comments, which have greatly improved this paper. This project was supported by the Engineering Research Center of Ministry of Education for Renewable Energy Infrastructure Construction Technology and Zhejiang Key Laboratory of Green Construction and Intelligent Operation & Maintenance for Coastal Infrastructure (Zhejiang University of Technology).

References

Aldaood, A., Bouasker, M., & Al-mukhtar, M. (2014). Impact of freeze-thaw cycles on mechanical behaviour of lime stabilized gypseous soils. *Cold Regions Science and Technology, 99*, 38–45.

ASTM. (2016). *Standard test method for unconfined compressive strength of cohesive soil* (ASTM D2166–16). West Conshohocken, USA: ASTM International.

ASTM. (2011). *Standard practice for classification of soils for engineering purposes (Unified Soil Classification System)* (ASTM D2487–11), ASTM International, West Conshohocken, Pennsylvania, USA.

Bahram, R., Khayat, N., & Nazarpour, A. (2020). Effect of nano-stabilizer on geotechnical properties of leached gypsiferous soil. *Geomechanics and Engineering, 23*(2), 103–113.

Bahrami, R., Khayat, N., & Nazarpour, A. (2021). Laboratory investigation on physical-mechanical characteristics and microstructure of a clayey gypsiferous soil in the presence of chemical accelerator. *KSCE Journal of Civil Engineering, 25*(9), 3273–3288.

Cai, H. B., Pang, C. Q., Hong, R. B., Yang, Z., & Li, M. K. (2025). Centrifuge modeling of ground thaw settlement during metro tunnel construction using AGF method. *Transportation Geotechnics, 55*, 101655.

Chen, H. X., Xue, Q. P., Feng, S. J., Zheng, Q. T., & Lyu, D. J. (2024). Durability of geopolymer cutoff wall backfill incorporating reactive MgO particles under dry-wet cycles. *Cement and Concrete Composites, 146*, 105406.

Chen, H. X., Xue, Q. P., Ma, Z. P., Gao, L., & Feng, S. J. (2023). Experimental study on barrier performance and durability under dry-

wet cycles of fly ash based geopolymer cutoff wall backfill. *Construction and Building Materials, 368*, 130415.

Chen, J. H., Wang, J. L., Wang, L. X., Li, H., & Chen, M. L. (2022a). Influence of freeze tube deviation on the development of frozen wall during long cross-passage construction. *Research in Cold and Arid Regions, 14*(4), 250–257.

Chen, K., Liu, X. F., Yuan, S. Y., Pan, S. X., Ma, J., & Jiang, G. L. (2022b). Shakedown behavior of saturated weathered red mudstone. *Soil Dynamics and Earthquake Engineering, 162*, 107497.

Feng, Z. Y., Wang, S. Y., Shi, Y. F., Zheng, X. C., & Qu, T. M. (2025). Development of a novel external load-controlled permeameter for sand-foam mixtures. *Tunnelling and Underground Space Technology, 164*, 106767.

Ghalandarzadeh, S., Courcelles, B., Boudreault, R., Arenson, L. U., & Maghoul, P. (2025). Effect of freeze-thaw cycles on engineering properties of nano-SiO_2 enhanced microbially induced calcium carbonate precipitation in kaolinite clay. *Cold Regions Science and Technology, 234*, 104459.

Ghimire, U., Bheemasetti, T. V., & Kim, H. J. (2025). Performance of stabilized copper mine tailings with freeze-thaw and wet-dry seasonal cycles. *Journal of Rock Mechanics and Geotechnical Engineering, 17*(3), 1418–1428.

He, P. F., Cao, H. T., Dong, J. H., Hou, G. L., Mu, Y. H., & Zhang, J. C. (2024). Effects of wet-dry-freeze-thaw cycles on the response of the frozen soil-composite geotextile interface in direct shear tests. *Case Studies in Thermal Engineering, 63*, 105217.

He, X. X., Xue, J. F., Liao, M. J., Wan, Y., Liu, X. L., Chen, Y. J., & Xue, Q. (2023). Strength and hygroscopic behavior of biopolymer-treated silty sand under remodeling and dry-wet cycles. *Construction and Building Materials, 408*, 133642.

Heydari, B., Khayat, N., & Nazarpour, A. (2024). Assessment of the immediate impact of anions and cations on clay soils resistance parameters case study (Garmsiri Project Iran). *Case Studies in Construction Materials, 20*, e03105.

Huang, H. J., Du, C. B., Yi, F., Chen, D. S., & Zhang, C. W. (2025). Microstructural and mechanical evolution of recycled fiber-reinforced tunnel slag concrete under wet-dry cycles. *Sustainable Chemistry and Pharmacy, 43*, 101905.

Huang, K., Fang, Z. Q., Cai, G. J., Shi, X. Z., Huang, K., He, Y., Duan, W., & Tian, N. C. (2024). Macro and microscopic characteristics of soft soil stabilized by Portland cement-soda residue under dry-wet cycling. *Construction and Building Materials, 428*, 136347.

Lang, L., Song, C. Y., Xue, L., & Chen, B. (2020). Effectiveness of waste steel slag powder on the strength development and associated micro-mechanisms of cement-stabilized dredged sludge. *Constructuction and Building Materials, 240*, 117975.

Li, B. Z., Min, F. L., Zhou, X., Zhang, N., Wang, X., & Yao, Z. H. (2024). Strength characteristics and solidification carbonization mechanism of MgO based shield tunneling centrifugal waste silt. *Construction and Building Materials, 447*, 138132.

Liu, C., Wu, Z. W., Garg, A., Qin, Y. H., Mei, G. X., Lyu, C., & Zhang, H. R. (2023). Experimental investigation for dynamic characteristics of paraffin-graphite based CPCM (composite phase change material) amended expansive soil under dry-wet cycles. *Construction and Building Materials, 404*, 133170.

Liu, Y. Z., Zhang, C. Z., Wu, K., & Liu, S. Y. (2024). Sustainable stabilization/solidification of Cd and Pb in industrially heavy metal-contaminated site soils using a novel binder incorporating bone meal and fly ash. *Construction and Building Materials, 416*, 135162.

Liu, Y., Wang, Z. X., Liu, X., & Wang, S. H. (2026). Review on the impact of freeze-thaw cycles on mechanical properties and durability of tunnel lining structures. *KSCE Journal of Civil Engineering, 30*(2), 100332.

Lu, J. F., & Jin, K. (2026). Analytical model for the seismic response of a shield tunnel with a heterogeneous grouting layer. *Soil Dynamics and Earthquake Engineering, 200*, 109872.

Lu, J. G., Deng, F., Liu, W. B., Gao, J. J., Liu, B. S., Zhou, X. X., & Zhang, Z. X. (2024). Impact of freeze-thaw cycles on the hydro-thermal-deformation behavior of silty clay: An experimental study. *International Communications in Heat and Mass Transfer, 158*, 107901.

Ma, X. F., Liu, Z. H., Wang, W. D., Wang, J. J., Lu, L. H., Zhou, D. Y., & Zhang, H. W. (2024). Characteristics of physical parameters and predictive modeling of mechanical properties in loess-like silty clay for engineering geology. *Engineering Geology, 339*, 107672.

Ma, Y. F., Bao, H., Yan, C. G., Lan, H. X., Peng, J. B., Zheng, H., Song, Z. T., & Liu, C. Q. (2023). Mechanical properties and microstructure evolution of two ecological slope-protection materials under dry-wet cycles. *Journal of Cleaner Production, 416*, 137833.

Min, F. L., Dai, J. J., Zhang, N., Ma, J. W., Zhang, L., & Li, B. Z. (2024a). Investigation into strength development mechanism of lime-modified dehydrated clay of slurry shield tunneling operation. *Construction and Building Materials, 438*, 137224.

Min, F. L., Yang, Y. W., Zhang, N., Ma, J. W., Shu, J. C., Zhang, Y. Z., & Wang, D. F. (2024b). Study on the effect of carbonation on the mechanical properties of lime modified waste clay. *KSCE Journal of Civil Engineering, 28*, 4668–4677.

Nasiri, H., Khayat, N., & Mirzababaei, M. (2021). Simple yet quick stabilization of clay using a waste by-product. *Transportation Geotechnics, 28*, 100531.

Nie, Y. P., Ni, W. K., Lyu, X. F., & Tuo, W. X. (2024). Exploring the mechanical behavior and microstructure of compacted loess subjected to dry-wet cycles and chemical contamination. *Journal of Rock Mechanics and Geotechnical Engineering, 16*(9), 3673–3695.

Ohadian, A., Khayat, N., & Mokhberi, M. (2024a). Microstructural analysis of marl soil stabilized with rejected municipal solid waste and nano-MgO. *Journal of Rock Mechanics and Geotechnical Engineering, 16*(8), 3258–3269.

Ohadian, A., Khayat, N., Mokhberi, M., & Horpibulsuk, S. (2024b). Soft clay modified with municipal solid waste and stabilized with nano-MgO for pavement subgrade and embankment fill applications. *Transportation Geotechnics, 46*, 101261.

Pang, Y. Y., Wang, H. L., Tang, Q., Yang, L., & Wang, Q. (2024). Enhancing cement mortar hydrophobicity against dry-wet cycling sulfate attack using stearic acid modified mica powder via high-temperature stirring. *Construction and Building Materials, 441*, 137556.

Qin, B., Li, X. A., Wang, L., Cao, R. R., & Chai, H. (2024). Model interpretation and microscopic characteristics of collapsibility evolution of compacted loess under dry-wet cycles. *Catena, 246*, 108413.

Shu, H., Yu, Q. B., Niu, C. C., & Wang, Q. (2025). The crack characteristics and microscopic mechanism of composite solidified soil under alternating wet-dry and freeze-thaw cycles. *Cold Regions Science and Technology, 235*, 104479.

Shu, H., Yu, Q. B., Niu, C. C., Liu, J., Xia, W. T., Sun, X., Wang, Z. X., & Wang, Q. (2023). Effect of dry-wet cycles on the mechanical properties of saline soil solidified with sulfur-free lignin and hydrophobic polymer. *Journal of Building Engineering, 76*, 107116.

Shu, H., Yu, Q. B., Niu, C. C., Sun, D., & Wang, Q. (2024). The coupling effects of wet-dry and freeze-thaw cycles on the mechanical properties of saline soil synergistically solidified with sulfur-free lignin, basalt fiber and hydrophobic polymer. *Catena, 238*, 107832.

Song, W. L., Zha, F. S., Zhu, Z. D., Xu, L., Kang, B., Yang, J. Q., & Pu, S. Y. (2024). Freeze-thaw resistance and deterioration mechanism of alkali-activated filling grouts prepared from full industrial solid wastes for tunnels. *Materials Today Communications, 41*, 111009.

Su, X. T., Huang, X. X., Chen, J., Saffari, P., Li, X. L., Li, Z., & Asadi, A. (2025). Strength characteristics and micro-mechanism of shield tunneling fine muck synergistically improved with fiber reinforcement and solid waste-based gelling agent. *Case Studies in Construction Materials, 23*, e05039.

Su, Y. H., Luo, B., Luo, Z. D., Xu, F., Huang, H., Long, Z. W., & Shen, C. P. (2023). Mechanical characteristics and solidification mechanism of slag/ fly ash-based geopolymer and cement solidified organic clay: A comparative study. *Journal of Building Engineering, 71*, 106459.

Sun, Y. L., Liu, Q. X., Xu, H. S., Wang, Y. X., & Tang, L. S. (2022). Influences of different modifiers on the disintegration of improved granite residual soil under wet and dry cycles. *International Journal of Mining Science and Technology, 32*(4), 831–845.

Sun, Y. L., Yu, C., Jiang, S. S., Chen, Y. G., Wang, Z. T., Duan, S. X., & Xie, J. B. (2025). Disintegration behaviors of red clay under wet-dry cycles. *Journal of Rock Mechanics and Geotechnical Engineering, 17*(9), 5875–5892.

Tang, N., Dultz, S., Gerth, D., & Klumpp, E. (2024). Soil colloids as binding agents in the formation of soil microaggregates in wet-dry cycles: A case study for arable Luvisols under different management. *Geoderma, 443*, 116830.

Wang, D. F., Min, F. L., Li, Z., Zhang, L., & Zhang, Y. Z. (2024a). Investigation into the properties of two-component backfilling grouts prepared by substituting bentonite with slurry from slurry shield

tunnelling treated by a hydrocyclone. *Tunnelling and Underground Space Technology, 154*, 106142.
Wang, D. F., Min, F. L., Lyu, H. J., Chen, J., Wang, B. T., & Zhang, J. F. (2023a). Recycling waste sand from slurry shield tunneling: A sustainable filter aid for waste slurry dehydration. *Journal of Cleaner Production, 383*, 135387.
Wang, J. X., Chai, J. R., Xu, Z. G., Geng, K. Q., & Zhang, P. Y. (2024b). A review of barrier properties of polymer-modified bentonite applied to vertical cutoff walls under dry-wet cycling and chemical erosion. *Journal of Water Process Engineering, 65*, 105759.
Wang, S. W., Wang, G. N., & Li, S. Y. (2024c). Study on shear surface morphology and failure mechanism of soil-rock mixture under wet-dry cycle action. *Physics and Chemistry of the Earth, 135*, 103659.
Wang, X. Q., Liu, N., Li, Z. Q., Han, Z., & Zou, W. L. (2023b). Hydro-mechanical properties of sludge stabilized with magnesium oxychloride cement-based multi-cementitious materials under influences of drying-wetting cycles. *Chinese Journal of Geotechnical Engineering, 45*(10), 2004–2013 (in Chinese).
Wang, X. Y., Yuan, D. J., Jin, D. L., & Su, W. L. (2020). Thermal and mechanical response of soil and tunnel during replacement of shield tail brush by freezing method. *KSCE Journal of Civil Engineering, 24*(5), 1632–1640.
Wang, Y. C., Liang, C., Zuo, Y. P., Du, Z. J., Wu, C. F., & Zhang, Z. (2026). Study on modified red mud-based grouting material and an experimental investigation on its control of sand-water gush in shield tunnels. *Transportation Geotechnics, 56*, 101797.
Xu, B., & Yi, Y. L. (2019). Soft clay stabilization using ladle slag-ground granulated blastfurnace slag blend. *Applied Clay Science, 178*, 105136.
Xu, Y., Wu, Y. J., Zhang, X. D., Chen, G., Zhang, Y. D., & Ji, J. W. (2023). Anti-clogging mechanism of freeze-thaw combined with step vacuum preloading in treating landfill sludge. *Environmental Research, 218*, 115059.
Xue, R. Y., Wang, K., Wang, Y. P., Jiang, M., Zhao, Q. L., & Jiang, J. Q. (2024). Effect of freeze-thaw frequency plus rainfall on As and Sb metal (loid)s leaching from the solidified/stabilized soil remediated with Fe-based composite agent. *Science of the Total Environment, 926*, 171844.
Yan, Q. X., Xu, Y. J., Yang, W. B., & Geng, P. (2018). Nonlinear transient analysis of temperature fields in an AGF project used for a cross-passage tunnel in the Suzhou Metro. *KSCE Journal of Civil Engineering, 22*(4), 1473–1483.
Yang, H., Zhu, J. F., Tao, Y. L., Wang, Z. Q., & Zheng, Q. Q. (2022). Effect of the dry-wet cycle on the performance of marine waste silt solidified by calcium carbide residue and plant ash. *Journal of Marine Science and Engineering, 10*(10), 1442.
Yin, S., Zheng, S. Y., Li, X. M., Wang, Z. L., Yan, P., He, Y., & Li, Y. R. (2025). Strength characteristics and microstructure of silty sand improved by red mud, lime and fly ash under dry-wet cycle. *Case Studies in Construction Materials, 22*, e04116.
Yu, C., He, C. B., Li, Z., Li, Y. A., Li, Y., Sun, Y. L., & Wu, Y. Q. (2024). Disintegration characteristics and mechanism of red clay improved by steel slag powder. *Construction and Building Materials, 444*, 137873.
Zeng, L. L., Bian, X., Zhao, L., Wang, Y. J., & Hong, Z. S. (2021). Effect of phosphogypsum on physiochemical and mechanical behaviour of cement stabilized dredged soil from Fuzhou, China. *Geomechanics for Energy and the Environment, 25*, 100195.
Zhang, B. Y., Zhang, J. H., & Sun, G. L. (2015). Deformation and shear strength of rockfill materials composed of soft siltstones subjected to stress, cyclical drying/wetting and temperature variations. *Engineering Geology, 190*, 87–97.
Zhang, H. G., Liu, T., Cui, Y. X., Wang, W. H., & Qing, C. R. (2025). Experimental study on the performance of basalt fiber combined with cement-based material solidified shield waste mud under the coupled effects of acid corrosion and dry-wet cycles. *Construction and Building Materials, 463*, 140110.
Zhang, P. Y., Fan, J., Xu, X. Y., Xu, Z. B., Yu, Y. L., Zhao, L., Qiu, H., & Cao, X. D. (2022a). Contrasting effects of dry-wet and freeze-thaw aging on the immobilization of As in As-contaminated soils amended by zero-valent iron-embedded biochar. *Journal of Hazardous Materials, 426*, 128123.
Zhang, S. J., Lai, Y. M., Zhang, X. F., Pu, Y. B., & Yu, W. B. (2004). Study on the damage propagation of surrounding rock from a cold-region tunnel under freeze–thaw cycle condition. *Tunnelling and Underground Space Technology, 19*(3), 295–302.
Zhang, W. J., Jin, D., & Yuan, J. (2024b). Speciation transformation and release of Cr(VI) in a GGBS-NaOH treated soil under acidic wet-dry cycle: Leaching characteristics and microscopic mechanisms. *Journal of Cleaner Production, 456*, 142424.
Zhao, Y., Zhang, H. R., Wang, G. Y., & Yang, Y. Q. (2024). The infiltration characteristics of expansive soil considering fracture under wet-dry cycle conditions. *Heliyon, 10*(17), e36840.
Zheng, J. Y., Li, J., Ling, L., Liu, X. M., Kong, S. L., Liao, H. Z., Liu, W. Z., Ning, P., & Lin, Z. (2020). Crystal regulation of gypsum via hydrothermal treatment with hydrogen ion for Cr(VI) extraction. *Journal of Hazardous Materials, 390*, 120614.
Zhou, J., Zhao, W. Q., & Tang, Y. Q. (2022). Practical prediction method on thaw deformation of soft clay subject to artificial ground freezing based on elaborate centrifuge modeling experiments. *Tunnelling and Underground Space Technology, 122*, 104352.
Zhou, R., Wang, B. T., Han, S. Y., Wang, D. Y., & Zhang, F. H. (2024b). Mechanisms of crack development and strength deterioration in compacted expansive soils under controlled wetting-drying conditions. *Engineering Failure Analysis, 159*, 108133.
Zhu, F. F., Jin, Y. C., & Xie, F. (2013). Research of characteristic and physical & mechanical indexes about red clay. *Resources Environmental & Engineering, 27*(3), 257–262 (in Chinese).
Zhu, J. F., Tao, Y. L., Xu, R. Q., Hao, Y., & Pan, B. J. (2022). Investigation on the optimal formulation and mechanism of marine organic silt improved with magnesium cement-based stabilizer. *Construction and Building Materials, 341*, 127233.
Zhu, J. F., Wang, Z. Q., Tao, Y. L., Ju, L. Y., & Yang, H. (2024). Macro-micro investigation on stabilization sludge as subgrade filler by the ternary blending of steel slag and fly ash and calcium carbide residue. *Journal of Cleaner Production, 447*, 141496.